Chinese Chemical Letters 34 (2023) 108124

Contents lists available at ScienceDirect

Chinese Chemical Letters

journal homepage: www.elsevier.com/locate/cclet

Photoactive donor-acceptor conjugated macrocycles: New opportunities for supramolecular chemistry

Shanyuan Zhong[a], Lingyun Zhu[a], Shuai Wu[a], Yuanming Li[a], Meijin Lin[a,b,*]

[a] Key Laboratory of Molecule Synthesis and Function Discovery, and Fujian Provincial Key Laboratory of Electrochemical Energy Storage Materials, College of Chemistry, Fuzhou University, Fuzhou 350116, China
[b] College of Materials Science and Engineering, Fuzhou University, Fuzhou 350116, China

ARTICLE INFO

Article history:
Received 31 October 2022
Revised 7 December 2022
Accepted 27 December 2022
Available online 29 December 2022

Keywords:
Conjugated macrocycles
Donor-acceptor
Photoactive
Supramolecular chemistry
Photoelectronic materials

ABSTRACT

The design and synthesis of photoactive macrocyclic molecules continue to attract attention because such species play important roles in supramolecular chemistry as well as photoelectronic applications. Donor-acceptor (D-A) conjugated macrocycles are an emerging class of photoactive molecules due to their D-A conjugated structural characteristics and tunable optical properties. In addition, the well-defined cavities in such D-A macrocycles endow them with versatile host-guest properties. In this review, we provide a comprehensive summary of D-A conjugated macrocycle chemistry, detailing recent progress in the area of synthetic methods, optical properties, host-guest chemistry and applications of the underlying chemistry to chemical sensors, bioimaging and photoelectronic devices. Our objective is to provide not only a review of the fundamental findings, but also to outline future research directions where D-A conjugated macrocycles and their constructs may have a role to play.

1. Introduction

Design and synthesis of new macrocycles with intriguing structures and peculiar functions (*e.g.*, optical, electronic and magnetic properties) are of great significance since their important roles in supramolecular chemistry and materials science [1–6]. The traditional macrocycles such as crown ether [7–10], cyclodextrins [11–14], calixarenes [15–18], cucurbiturils [19–21], pillararenes [22–25] and their structurally similar scaffolds usually possess tunable cavities for binding guests but no other photoelectronic functions for further applications. Moreover, their skeletons are incapable of being changed and functional substituents can be introduced only on their portals. Therefore, it is challenging to create a class of customizable functional macrocycles with a wide range of cavity sizes and diverse functions.

Donor-acceptor (D-A) conjugated molecules containing alternate donor (D) and acceptor (A) motifs are an emerging class of functional molecules with tunable optical properties, electronic structures as well as redox properties [26–30], which have potential applications in various fields such as organic optoelectronic devices [31–36], sensors and bioimaging [37–42]. In these molecules, the electronic-rich building blocks (called D motifs) generally govern the highest occupied molecular orbitals (HOMOs), while the electron-deficient building blocks (called A motifs) determine the lowest unoccupied molecular orbitals (LUMOs). More importantly, due to the tailorable HOMO-LUMO energy gaps and facilitated electron transports in the π-conjugations, these D-A conjugated molecules are always photoactive and could be excited by the UV-vis lights. Recently, chemists have introduced this design strategy into the synthetic macrocycles, and rolled such linear D-A conjugated molecules into different macrocycles to develop a new class of functional macrocycles named "D-A conjugated macrocycles (DACMs)", which is anticipated to combine the bilateral advantages of host-guest properties from synthetic macrocycles and photoactive properties from the D-A conjugated molecules.

Indeed, a myriad of D-A π-conjugated macrocycles with different applications has been reported in the past decades. Compared with the traditional macrocycles, the D-A π-conjugated macrocycles possess the following unique characteristics: (1) Their cyclic structures are often shape-persistent but controllable, which are beneficial towards supramolecular self-assembly and accommodation of guest molecules with electronic activity [43–45]. (2) Their electronic structures as well as photoactive properties could be modulated by their π-conjugations and introduction of the appropriate donor and acceptor units [46,47]. (3) Compared with linear conjugated molecules, macrocycles can not create charge defects thanks to lacking end-groups [48–51]. Accordingly, such photoac-

* Corresponding author at: Key Laboratory of Molecule Synthesis and Function Discovery, and Fujian Provincial Key Laboratory of Electrochemical Energy Storage Materials, College of Chemistry, Fuzhou University, Fuzhou 350116, China.
E-mail address: meijin_lin@fzu.edu.cn (M. Lin).

https://doi.org/10.1016/j.cclet.2022.108124
1001-8417/

tive DACMs hold a broad application prospect in supramolecular chemistry and functional materials.

In this review, we provide a comprehensive summary of DACMs chemistry. The synthesis of DACMs is presented by the different linkages between their D and A motifs, such as vinylene, ethynylene, arylene, B/N-containing linkers in their cyclic backbones. Unique optical properties with controllable electronic structures as well as rich host-guest chemistry are also illustrated to shed light on the relationships between their structures and properties. Moreover, their potential applications in chemical sensors, bioimaging, and photoelectronic devices especially in organic photovoltaics and organic light-emitting diodes are also discussed. Our objective is to provide not only a review of the fundamental findings, but also to outline future research directions where DACMs and their constructs may have a role to play.

2. Synthesis of DACMs

In the past decades, a variety of D and A units have been introduced into the macrocycles to gain tunable optical and electronic structures. In general, D and A moieties are connected *via* π-systems, such as vinylene, ethynylene, and arylene [52,53]. Also, different D and A units can be connected directly to form DACMs in alternating fashions, as illustrated in Fig. 1, in which the blue color represents the D while the flesh color represents the A [54].

2.1. Vinylene-linked macrocycles

As we know, the vinylene-linked π-conjugations could be commonly created by the Wittig reactions [55], McMurry cross-coupling reactions [56], and glyoxylic Perkin condensation reactions [57,58]. In 2017, a D-A structural carboxyfunctionalized 1,6-pyrenophane-tetraene macrocycle was firstly reported by Robert and co-workers (Fig. 2) [59] *via* glyoxylic Perkin condensation reactions. 1,6-Pyrenylenediglyoxylic acid **1** was reduced to 1,6-diacetic acid **2** under H_3PO_2/NaI. Glyoxylic Perkin condensation was taken place between **1** and **2** under high dilution conditions to afford macrocycle **3** in *ca.* 25% isolated yield. By changing the linkers,

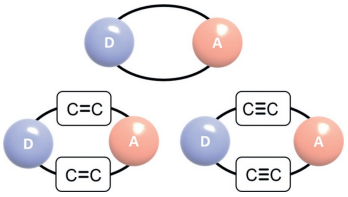

Fig. 1. Schematic of three connection methods of D-A conjugated macrocycle mentioned in this review.

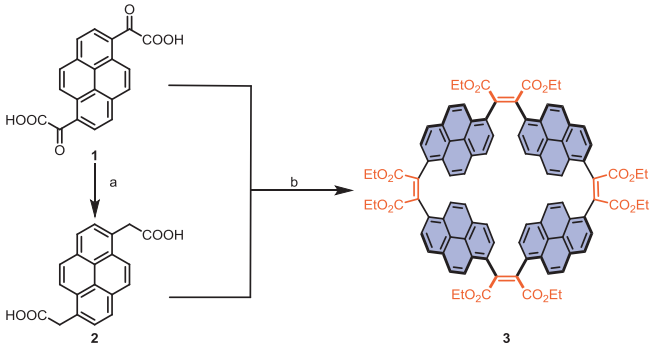

Fig. 2. Synthesis of macrocycle **3**. Conditions: (a) H_3PO_2, NaI, AcOH, reflux, 16 h, 92%; (b) Ac_2O, NEt_3, THF, reflux, 72 h, then add EtOH, EtBr, DBU, reflux, 24 h, 25%. DBU = 1,8-diazabicyclo[5.4.0]undec-7-ene.

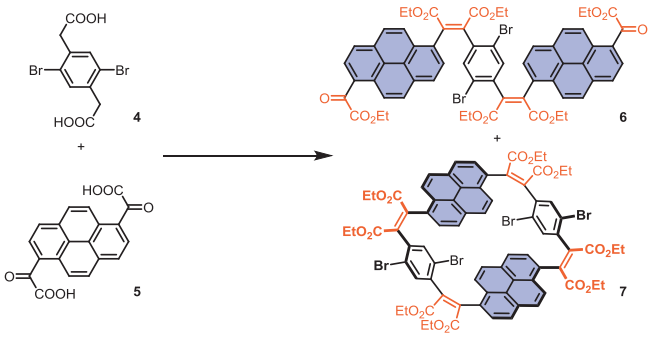

Fig. 3. Synthesis of linear bismaleate **6** and conjugated macrocycle **7**. Conditions: Ac_2O, NEt_3, THF, reflux, 16 h, then EtBr, EtOH, DBU, reflux, 24 h. Reaction conditions: (A) 8 equiv. of **5**, concentrated, **6**: 0%, **7**: 25%; (B) Stoichiometric, high dilution, **6**: 0%, **7**: 69%.

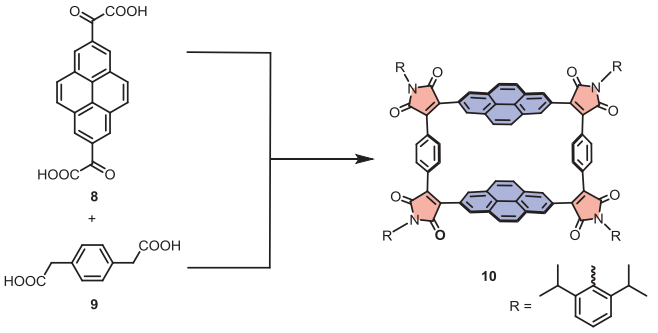

Fig. 4. Synthesis of DACMs **10**. Conditions: Ac_2O, Et_3N, THF, reflux, then 2,6-diisopropylaniline, 58%.

when a large excess of diglyoxylic acid **5** was reacted with dibromophenylene diacetic acid **4** in an attempt to generate linear three-block biamaleate **6** (Fig. 3) [60]. Unexpectedly, a D-A conjugated macrocycle **7** was synthesized in *ca.* 25% yield, which can reach up to 69% under high dilution conditions.

Inspired by these unexpected results, our group developed a facile and efficient approach for the synthesis of imides embedded DACMs **10** *via* glyoxylic Perkin condensation and imidization reaction under mild conditions recently [61]. As shown in Fig. 4, the conformationally adaptive macrocycle **10** was prepared by glyoxylic Pekin condensation of precursors pyrenylene-2,7-digloxylic acid **8** and 1,4-diphenylenediacetic acid **9** using Et_3N as the catalyst, and followed by an imidization with 2,6-diisopropylaniline. Our group also swapped the pyrenylene-2,7-digloxylic acid **8** with pyrenylene-1,6-digloxylic acid to generate different macrocycles *via* a similar synthetic procedure, and the related optical property will be demonstrated in Section 3 [52]. Notably, the present macrocyclization yield (58%) has a good lead over other π-conjugated macrocycles prepared by metal catalysis (*ca.* 5%-52%), which might be related to the formation of dynamic covalent bonds during the Perkin condensations under thermodynamic control [62,63]. Due to the dynamic and reversible bonding characteristics, it is helpful to generate the low-energy macrocyclic intermediates. More importantly, these dynamic and reversible bonds could be fixed by the following imidization reactions, which is further in favour of the formation of the stable **10** in high yields. Thus, dynamic covalent methods are indeed mighty strategies to carry out the macrocyclization process.

2.2. Ethynylene-linked macrocycles

Sonogashira cross-coupling [64,65], Glaser homo-coupling and Eglington coupling reactions are the general methods to syn-

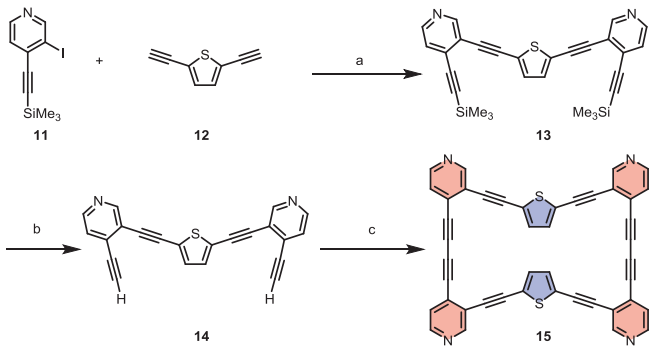

Fig. 5. Synthesis of macrocycle **15**. Conditions: (a) $PdCl_2(PPh_3)_2$, CuI, toluene, 20 °C, 5 d (54%); (b) 1 mol/L $(^nBu)_4NF$, THF, H_2O, 20 °C, 20 h (88%); (c) $[Cu_2(OAc)_4]2H_2O$, pyridine, 20 °C, 7 d (46%).

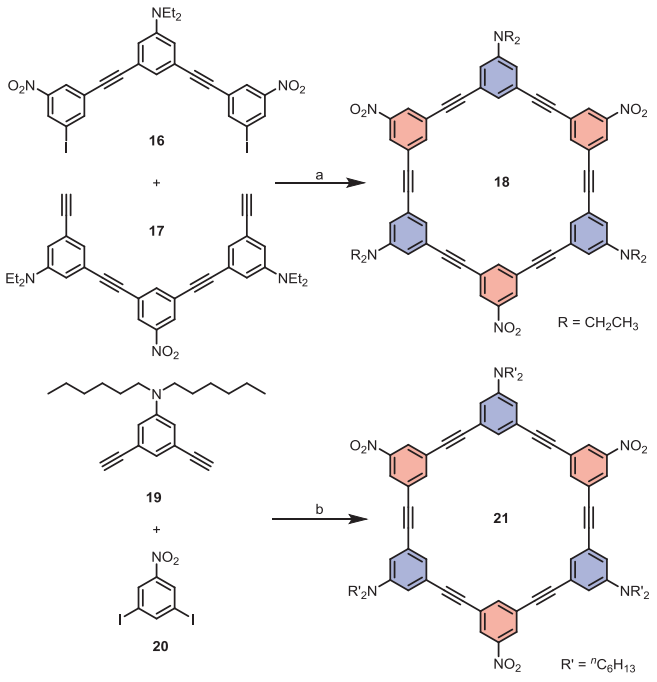

Fig. 6. Synthesis of macrocycles **18** and **21**. Conditions: (a) $Pd(PPh_3)_4$, CuI, $^iPr_2NH$, THF; (b) $Pd(PPh_3)_4$, CuI, C_6H_6, NEt_3.

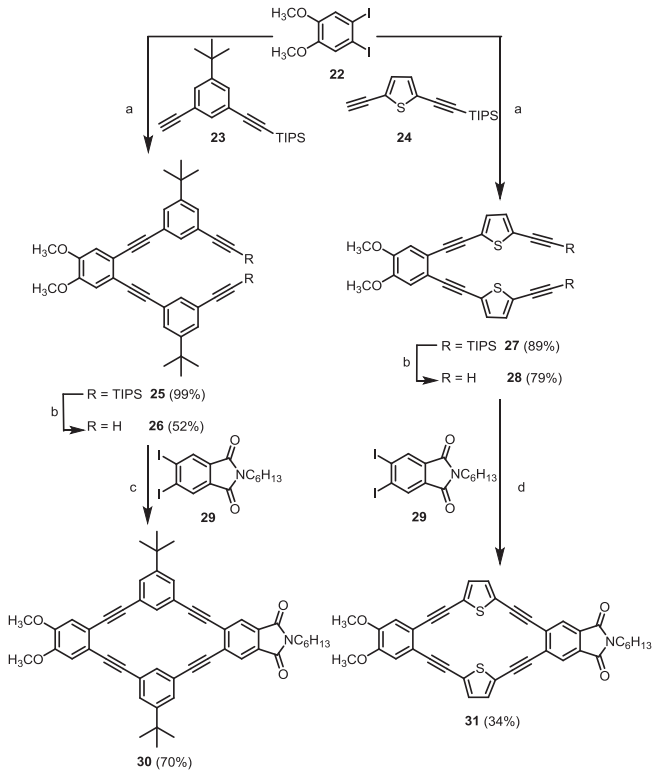

Fig. 7. Synthesis of macrocycles **30** and **31**. Conditions: (a) $Pd(OAc)_2$, PPh_3, CuI, HN^iPr_2; (b) TBAF, THF; (c) $Pd(P^tBu_3)_2$, NEt_3, toluene; (d) $Pd(P^tBu_3)_2$, DABCO, toluene. TBAF = tetrabutylammonium fluoride, DABCO = *N*,*N*-dimethylethanolamine.

thesize D-A structural ethynylene macrocycles [66]. In 2004, a dehydroannulene-type cyclophane **15** furnished with fluorescence ion sensory properties was synthesized by the Baxter group *via* Eglinton/Galbaraith coupling, in which the ring skeleton was composed of thiophene as donor units and pyridine as acceptor units with ethynylene linkage (Fig. 5) [67]. Silylated-intermediate **13** was obtained by coupling **12** and **11** under Sonogashira coupling reactions. **14** was desilylated with TBAF in aqueous THF and followed by a terminal alkyne coupling under high dilution afforded the target D-A conjugated macrocycle **15**.

In 2005, Traber *et al.* applied palladium-copper-catalyzed Sonogashira coupling to construct arylene ethynylene macrocycles (Fig. 6) [68]. Bimolecular macrocyclization between precursors **16** and **17** in one-pot under the catalysis of $Pd(PPh_3)_4$/CuI was performed to afford product **18**. However, the purification was problematic due to the poor solubility of **18**. In this case, two hexyl substituents were introduced in amine group to change this situation. The desired macrocycle **21** was attained by reacting **19** and **20** under Sonogashira coupling conditions in a yield of 20% after purification.

Leu *et al.* have developed *m*-phenylene-bridged cross-conjugated macrocycle **30** and 2,5-thiophene-bridged macrocycles **31** *via* Sonogashira cross-coupling reaction (Fig. 7) [53]. Sonogashira coupling reaction was taken place between TIPS-protected *m*-phenylene ethynylene monomer and *o*-diiodoarene, treating with TBAF to deprotect leading to **26** and **28** with moderate yields after purification. Notaly, macrocyclization was accomplished by using $Pd(P^tBu_3)_2$ as catalyst under copper-free conditions which plays a critical role in improving the yield of resulting macrocycles. Similar synthetic procedures were capitalized to generate 2,5-thiophene-containing macrocycle **31**. It was found that the cross-conjugated bridges are conducive to charge transfer.

Phulwale *et al.* utilized the Sonogashira coupling reaction for the construction of the triangular shape-persistent fully conjugated macrocyclic structures **37** and **39** based on the building block phenanthrylene (Fig. 8) [69]. The reaction of the terminal alkyne **32** and aryl halide **33** catalyzed by $Pd(PPh_3)_4$ and CuI system was employed to afford the open-chain precursor and followed by the Sonogashira cross-coupling reaction between the resultant and acetylene gas under a dilute concentration leading to macrocyclic molecule **34**. The D-A conjugated macrocycle **35** was obtained after deprotection by TFA. Diamine **36** and **38** were applied to convert *o*-quinone into dibenzophenazine and dibenzoquinoxaline respectively, which perform as acceptor units in macrocycles **37** and **39**.

The naphthalenediimide-based enantiomeric pair **42** and **43** with D-A system reported by Takeuchi were synthesized by Sonogashira coupling reaction (Fig. 9) [70]. 2,6-Dibromonaphthalenediimide **40** and 1,8-diethynylanthracene **41** were subjected to intermolecular macrocyclization under the catalysis of $Pd(PPh_3)_4$ and CuI in refluxing THF, leading to the final products in 15% isolated yield. Interestingly, the enantiomeric pair exhibited absorption and fluorescence response in varied tempera-

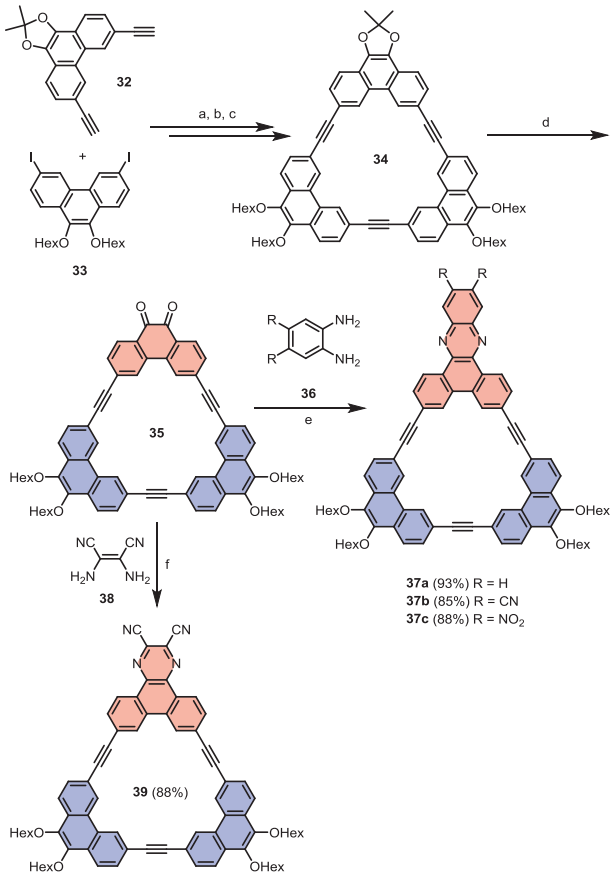

Fig. 8. Synthesis of D-A macrocycles **37** and **39**. Conditions: (a) $Pd(PPh_3)_4$, CuI, Et_3N, THF, 70 °C, 3 h, 58%; (b) acetylene, $Pd(PPh_3)_4$, CuI, Et_3N, THF, 70 °C, 3 h, 48%; (c) $Na_2S{\cdot}H_2O$, toluene, MGE, 150 °C, 12 h; (d) TFA, DCM, H_2O, rt, 12 h, 83%; (e) **36**, PTSA, AcOH, EtOH, DCM, 110 °C, 12 h; (f) **38**, PTSA, AcOH, EtOH, DCM, 100 °C, 12 h. PTSA = *p*-toluenesulfonamide, TFA = trifluoroacetic acid.

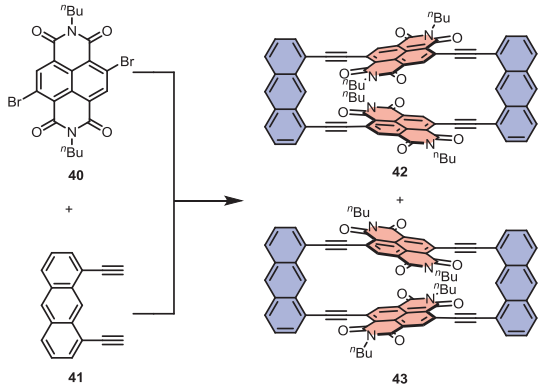

Fig. 9. Synthesis of enantiomeric pairs **43** and **44**. Conditions: $Pd(PPh_3)_4$, CuI, THF, reflux, 24 h.

tures, which holds great prospective in the area of molecular thermometer.

In 2021, dos Santos and co-workers demonstrated the construction of a vinylene-ethynylene-fused conjugated macrocycle **45** for the application of organic electronics based on thiophene moiety *via* a McMurry coupling process (Fig. 10) [71]. The Sonogashira coupling was carried out under $Pd(PPh_3)_4$ and CuI to give the precursor **44**, and then, intermolecular macrocyclization between two **44** fragments was performed *via* McMurry coupling to afford the final cyclic structure **45** in 17% yield.

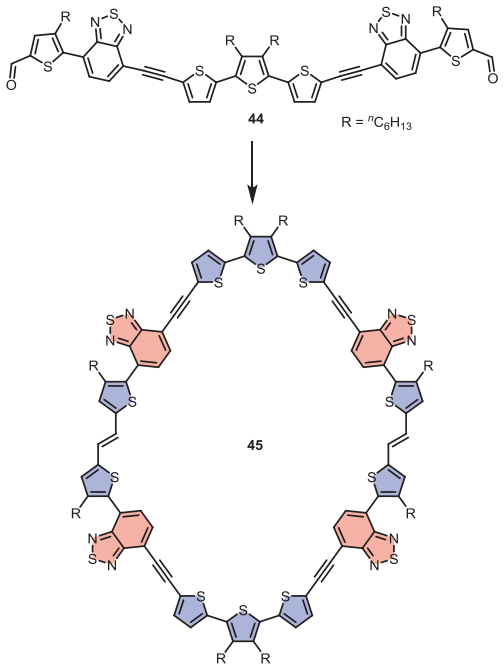

Fig. 10. Synthesis of macrocycle **45**. Conditions: $TiCl_4$, Zn, pyridine, THF, reflux, 22%.

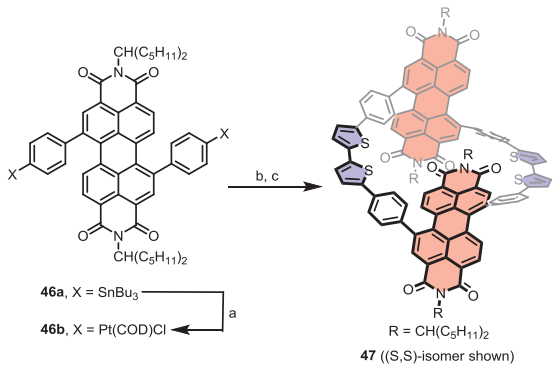

Fig. 11. Synthesis of macrocycle **47**. Conditions: (a) $Pt(COD)Cl_2$, toluene, 100 °C, 24.5 h, 45%; (b) 5,5′-bis(trimethylstannyl)-2,2′-bithiophene, THF, 50 °C, 40 h; (c) PPh_3, toluene, 100 °C, 24 h, 8% (2 steps). COD = 1,5-cyclooctadiene.

2.3. Arylene-linked macrocycles

The construction of arylene and/or heteroarylene DACMs in alternating patterns mainly depends on multinuclear macrocyclic Pt complexes and follow by a reductive elimination process. In 2015, the building blocks of thiophene and perylene diimide (PDI) derivative were utilized by Ball and co-workers to synthesize chiral conjugated macrocycles in an alternating D-A-D-A pattern *via* cyclic platinum complex [72]. The A fragment, 1,7-diphenyl-PDI possesses high stability of n-type charge carrier and excellent electronic characteristics, which is an ideal building block to construct optoelectronic materials. As shown in Fig. 11, stannylated **46a** was treated with $PtCl_2(COD)$ to afford **46b**. The conversion of **46b** into four-cornered tetraplatinum macrocycle-intermediate was implemented by reacting with 5,5′-bis(trimethylstannyl)-2,2′-bithiophene for 40 h. The target macrocycle was produced through a reductive elimination by treating with PPh_3 in a yield of 8%. The linkage at 1,7-position of diphenyl-PDI results in three stereoisomers, enantiomers (*S*,*S*) and (*R*,*R*) and *meso* isomers (*R*,*S*). X-ray analysis of single crystals indicated that the *meso* isomer possesses a larger ring strain owing to the bowl-shaped linker. Based

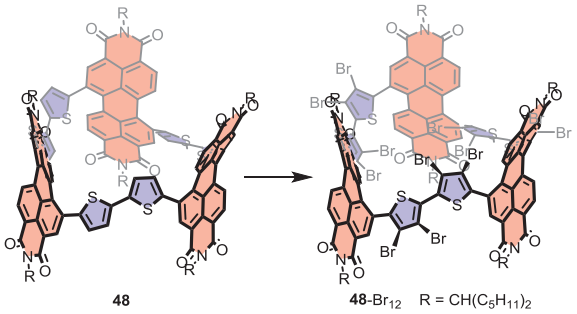

Fig. 12. Synthesis of macrocycle **48**-Br_{12}. Conditions: Br_2, I_2, CH_2Cl_2, r.t.

on this result, Liu and co-workers replaced the units bithiophene with trithiophene to design new macrocycles *via* theoretical analysis [73]. Trithiophene possesses a red-shift absorption with respect to bithiophene, which is expected to increase the ability of harvesting light in the newly designed macrocycles. Furthermore, NH_2 and NO_2 groups were incorporated into the trithiophene moiety to explore the influence of absorption spectra by employing theoretical calculation.

In 2018, Zhang's group further built up a trimer macrocycle **48** with stannylated 1,7-dithienyl-PDI subunit through a platinum complex (Fig. 12) [74]. Subsequently, to endow the macrocycle with the ability of self-assembly through halogen bonding interactions, bromine atoms were introduced into the thiophene rings to afford the functionalized **48**-Br_{12}. As expected, the brominated macrocycle can assemble into a capsular structure, which can be applied as active layer in field transistor devices. At the same time, they also integrated helical perylene diimide ribbons into macrocyclic backbone **50** and **52** through the same synthetic pathway as that of **47** to explore the relationship between molecular conformation and electronic property (Fig. 13) [75].

Interestingly, Würthner reported an ingenious D-A conjugated macrocycle **57** in 2021 that the PDI units located inside the macrocycle, in which the ring backbone was constructed based on oligothiophene with phenylene as linkages (Fig. 14) [76]. Imidization was performed between **53** and amines **54** under microwave irradiation and high temperature. Pt-intermediate **55c** was obtained after stannylation and Sn-Pt exchange with $Pt(COD)Cl_2$. Intermolecular cross-coupling reactions between Pt-mediated **55c** and stannylated **56** were fulfilled to give target products **57**. It is worth noting that elevated temperature plays a decisive role in ensuring a *syn*-conformation of thiophene units. In 2022, Würthner further utilized the same building blocks PDI and thiophene to construct a series of D-A conjugated half-cycles **63**-**66** *via* the same synthetic pathway [77]. As shown in Fig. 15, ring closure was carried out by the combination of PDI-thiophene precursor **58** and stannylated α-oligothiophene structures bearing two (**59**) to five (**62**) thiophene subunits under high-dilution conditions in order to suppress the intermolecular polymerization. They also attached PDI units extraannularly the thiophene macrocycle *via* an oxidative coupling pathway to investigate the influence on supramolecular assembly with the introduction of PDI segments [78].

Similar to the synthesis of **48**, Li created a diketopyrrolopyrrole-based D-A conjugated macrocycle **69** which can be utilized as non-fullerene acceptor to construct organic solar cells (Fig. 16) [54]. The macrocyclic platinum complex **68a** was prepared by reacting **67** with $[PtCl_2(COD)]$. Treated with dppf and underwent a reductive elimination process with PPh_3 yielded the required macrocycle **69**. The yield after purification was up to 16%.

The synthesis of twisted macrocycle **72** with significant fluorescence solvatochromism was carried out by Itami through Suzuki–Miyaura coupling [79]. As shown in Fig. 17, the building block with

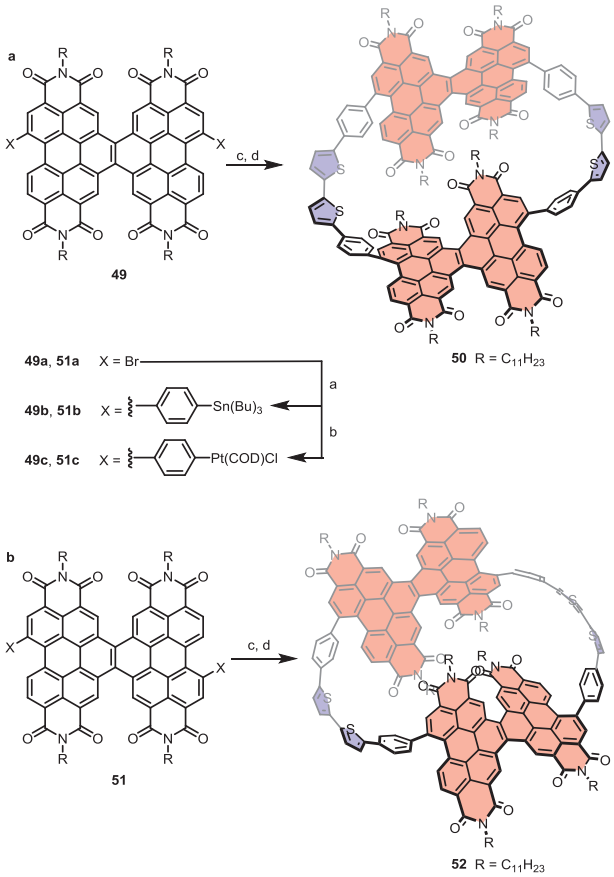

Fig. 13. Synthesis of macrocycles **50** and **52**. Conditions: (a) 1,4-Bis-(tributylstannyl)benzene, P-(2-furyl)$_3$, Pd_2dba_3, THF, 55 °C, 12 h; (b) $Pt(COD)Cl_2$, toluene, 100 °C, 12 h; (c) 5,5′-Bis(tributylstannyl)-2,2′-bithiophene, THF, 55 °C, 40 h. (d) PPh_3, toluene, 100 °C, 12 h.

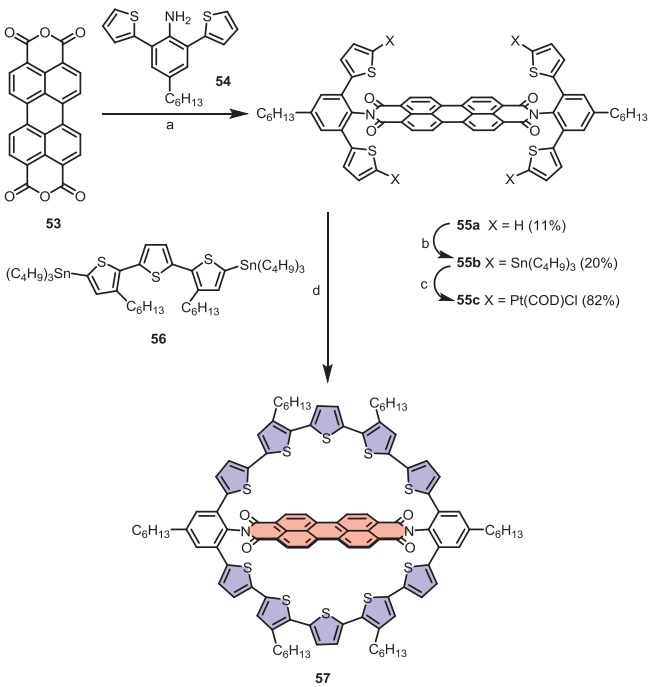

Fig. 14. Synthesis of macrocycles **57**. Conditions: (a) $Zn(OAc)_2$, imidazole, microwave irradiation; (b) $Sn(C_4H_9)Cl$, *n*-BuLi, THF, r.t., overnight; (c) $Pt(COD)Cl_2$, toluene, 95 °C; (d) toluene, 75 °C, overnight, then dppf, CH_2Cl_2, r.t., 6 h, then *m*-xylene, 120 °C, overnight. dppf = 1,1'-bis(diphenylphosphino)ferrocene.

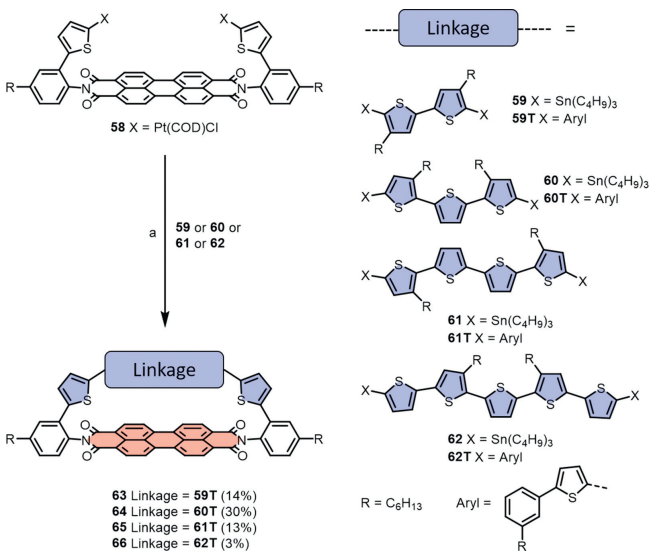

Fig. 15. Synthesis of macrocyclic D-A dyads **63**, **64**, **65** and **66**. Conditions: (a) toluene, 75 °C, overnight, then dppf, CH_2Cl_2, r.t., 6 h, then *m*-xylene, 120 °C, overnight.

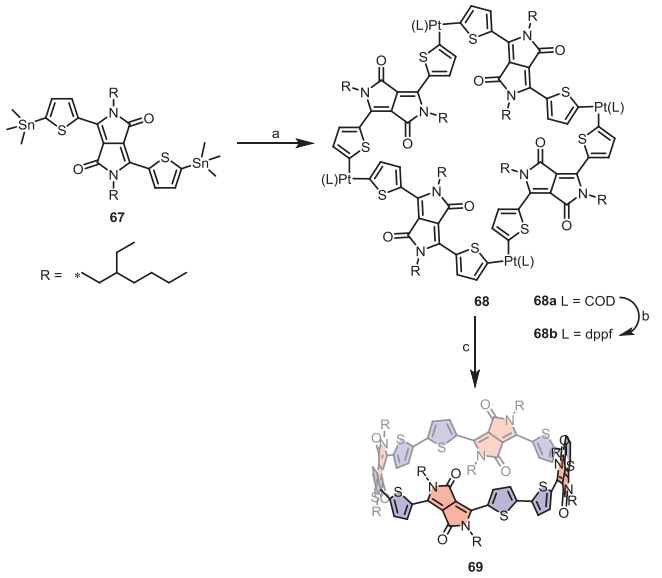

Fig. 16. Synthesis of D-A conjugated macrocycle **69**. Conditions: (a) $[Pt(COD)Cl_2]$, THF, 70 °C, 24 h; (b) (dppf), CH_2Cl_2, r.t., 12 h; (c) PPh_3, toluene, 110 °C, 12 h, yield 16% after three steps.

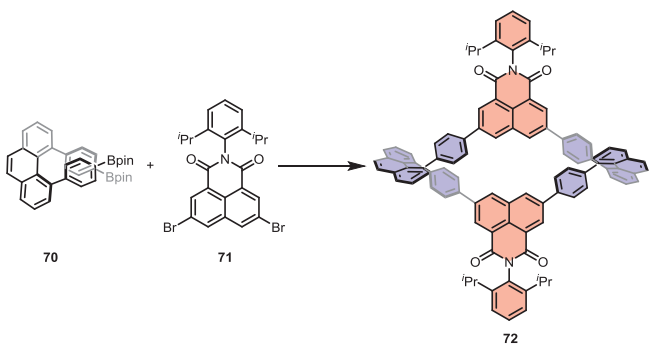

Fig. 17. Synthesis of macrocycle **72**. Conditions: $Pd(OAc)_2$, XPhos, NaOH, 1,4-Dioxane, 80 °C, 16 h, 8%.

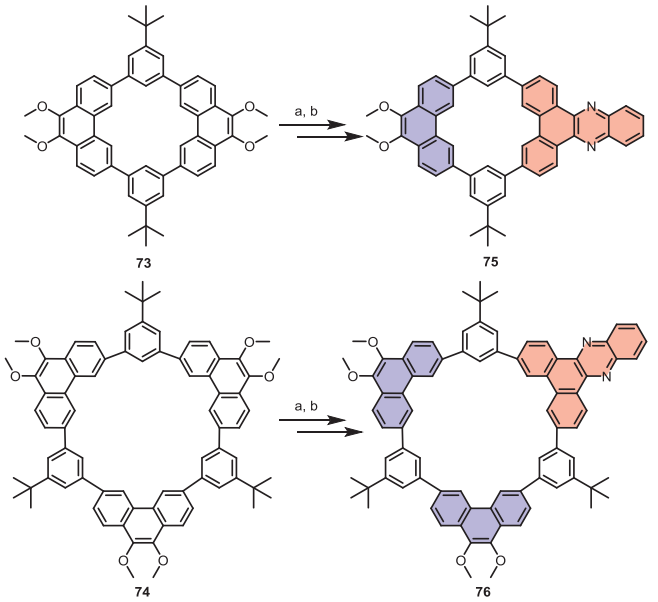

Fig. 18. Synthesis of macrocycles **75** and **76**. Conditions: (a) $Ce(NH_4)_2(NO_3)_6$, THF/ACN, r.t., 30 min; (b) 1,2-Diaminobenzene, glacial acetic acid, chloroform, 70 °C, 16 h.

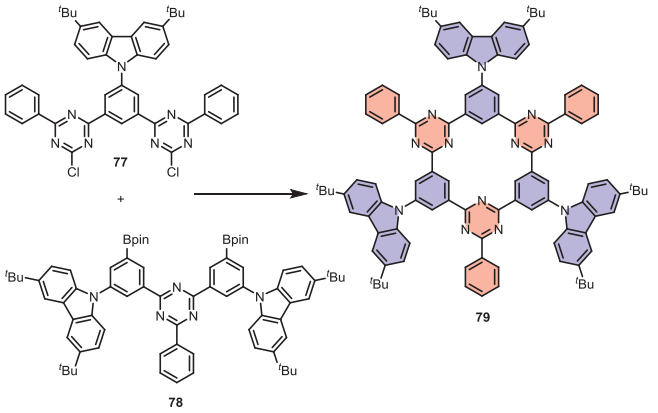

Fig. 19. Synthesis of macrocycle **79**. Conditions: $Pd(PPh_3)_4$, Cs_2CO_3, THF, reflux, 18%.

axially chirality, 4,5-diphrnylphenanthrene with diboronic acids, coupled with 3,6-dibromonaphthalimide through quadruple Pd-catalyzed Suzuki–Miyaura cross-coupling, leading to the nonplanar aromatic macrocycle **72** with 8% yield.

Very recently, Wang *et al.* have made an available approach for the construction of DACMs *via* post-functionalization (Fig. 18) [80]. On the basis of their previous results, the D-A system was incorporated into the synthesized conjugated macrocycles **73** and **74** by oxidizing methoxy groups and then condensation with aniline to generate **75** and **76**. The resulted dibenzo[*a*,*c*]-phenazine moieties acted as acceptor units, which endow the newly designed macrocycles with a narrowing energy gap.

The Shikita group reported the formation of an alternating macrocycle **79** with cyclo-*meta*-phenylene motif comprising of three 5-(*N*-carbazolyl-phenylen-1,3-diyl) and three 6-phenyl-1,3,5-triazin-2,4-diyl *via* Suzuki–Miyaura cross coupling reaction (Fig. 19) [81]. Macrocyclization was carried out between trimeric dichloride **77** and diboronate precursor **78** under dilution conditions and the target product **79** was generated in an 18% isolated yield.

Coupling reactions play a significant role in synthesizing DACMs, but there still exist disadvantages. It is inevitable to form undesired oligomers and polymers during the process of macrocy-

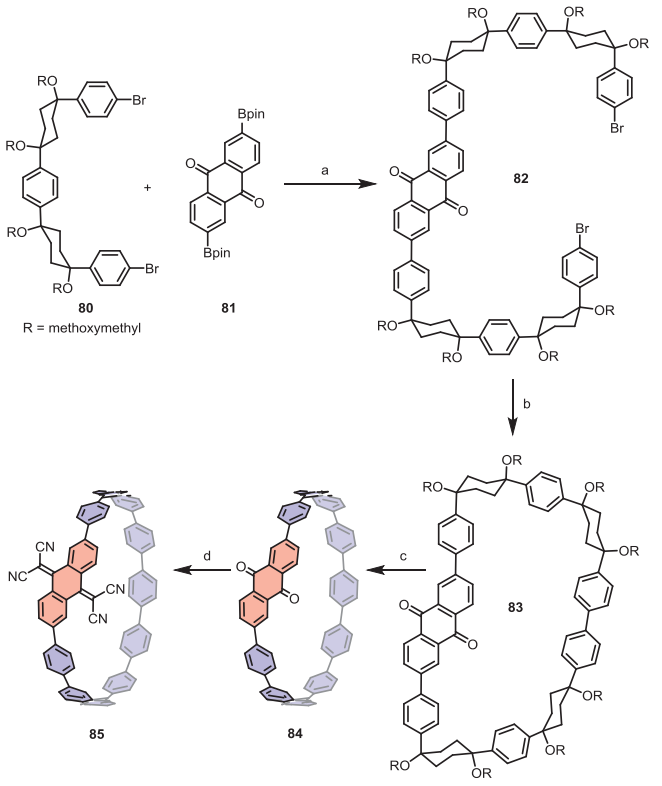

Fig. 20. Synthesis of **84** and **85**. Conditions: (a) $Pd(PPh_3)_4$, Na_2CO_3, $^nBu_4NBr$, THF, reflux, 41 h, 76%; (b) $Ni(COD)_2$, 2,2′-bipyridyl, THF, reflux, 25 h, 56%; (c) $NaHSO_4{\cdot}H_2O$, *o*-chloranil, *m*-xylene, water, 150 °C, 75 h, 27%; (d) Malononitrile, $TiCl_4$, pyridine, CH_2Cl_2, 0 °C to r.t., 26 h, 81%.

clization. In this regard, a highly dilute concentration of reactants is needed to inhibit the formation of linear conjugated molecules.

2.4. Cycloparaphenylene (CPP)-based macrocycles

Cycloparaphenylene (CPP) as emerging aromatic macrocycles comprised of arylene and heteroarylene based on coupling reactions [82]. The curved macrocycles **84** and **85** designed by Itami were synthesized *via* stepwise coupling reactions (Fig. 20) [83]. The Suzuki−Miyaura cross-coupling reaction between **80** and **81** were taken place to achieve C-shaped precursor **82** in a yield of 76%. The final structure **84** was obtained by means of Ni-mediated cyclization and followed by an aromatization process. The conversion of anthraquinone (AQ) into tetracyanoanthraquinodimehane (TCAQ) endows acceptor moiety of **85** with a strengthened electron-withdrawing ability.

Jasti achieved a series of aza[8]cycloparaphenylenes *via* replacing the acceptors by the alkylated pyridine moieties in 2015 [84]. Macrocyclization was carried out between **86** and **87** *via* a palladium-catalyzed Suzuki cross-coupling process (Fig. 21). The resulting cyclic compound **88** was then submitted to a reductive aromatization, leading to two nitrogen-doped nanohoop structures **89** and **90**. Alkylation of **89** and **90** was conducted respectively to obtain the D-A hoops **91** and **92**. The key steps are the construction of U-shaped precursors **86** and **87** on account of ring strain. In those structures, the alkylated pyridine ring acts as an acceptor while the oligophenylene chain acts as a donor unit.

Then, Jasti further reported a nitrogen-doped [6]CPP nanohoop **96** (Fig. 22) with higher ring strain owing to the smaller diameter by contrast with **91** and **92** in 2015 [85]. The precursor **93** was obtained through lithium-halogen exchange and Miyaura borylation. Macrocyclization was carried out by means of sequential

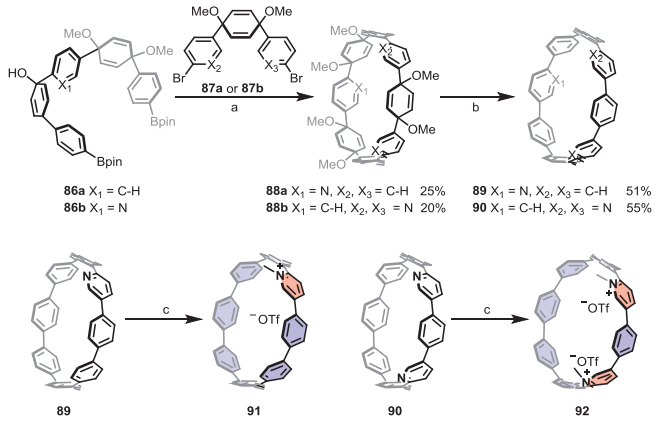

Fig. 21. Synthesis of D-A aza[8]CPPs **91** and **92**. Conditions: (a) K_3PO_4, SPhos Pd G2, 80 °C; (b) sodium napthalenide, THF, 78 °C; (c) MeOTf, SPhos Pd G2 = chloro(2-dicyclohexylphosphino-2′,6′-dimethoxy-1,1′-biphenyl)(2′-amino-1,1′-biphenyl-2-yl)palladium(II).

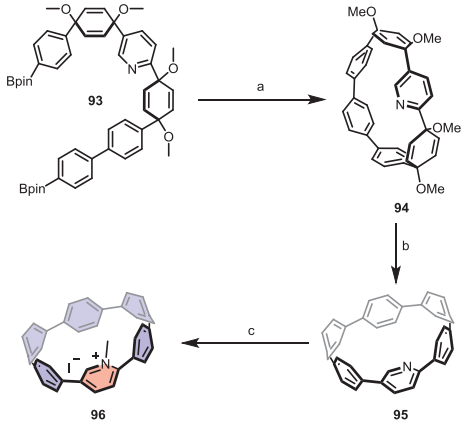

Fig. 22. Synthesis of **96**. Conditions: (a) $Pd(PPh_3)_2Cl_2$, KF, $B(OH)_3$, O_2, THF/H_2O, 51%; (b) i. sodium naphthalenide, THF, -94 °C; ii. I_2, THF, 45%; (c) Methyl iodide, CH_2Cl_2, 100 °C, μW, 83%.

Miyaura borylation and treating with an oxidative homocoupling under mild conditions to give **95** with a yield of 51%. The key to constructing the highly strained aza[6]CPP **95** lies in the strategy of boronate homocoupling reaction.

Wang and co-workers reported the construction of **100**, **101** and **102** bearing one, two, or three 2,7-bis(2-thienyl)-*9H*-fluoren-9-one (TFOT) units (Fig. 23) [86]. The precursors **97** was submitted to $Ni(COD)_2$-mediated intramolecular homocoupling and followed by an oxidative aromatization with DDQ afforded the target product **100** bearing one TFOT unit in a yield of 86%. Similarly, macrocycles **101** and **102** were generated *via* $Ni(COD)_2$-mediated coupling reaction of **97a** and **97b** and followed by an oxidative aromatization process with yields of 7% and 14%, respectively.

Suzuki macrocyclization was applied for the construction of CPP-based D-A macrocycle **106** with bright orange-emitting (Fig. 24) [87]. The acceptor unit, benzothiadiazole (BT) fragment was introduced by the reaction of **103** and 4,7-dibromobenzo[*c*]-1,2,5-thiadiazole **104** under Suzuki coupling conditions. The resulting product **105a** was subjected to triethylsilyl deprotection and followed by a reductive aromatization process under H_2SnCl_4 to generate the final macrocycle **106** in 22% isolated yield.

The Tan group recently reported the synthesis of D-A hoop **108** (Fig. 25) containing *tetra*-benzothiadiazole (TB) acceptors units *via* platinum-complex intermediate, in which the macrocycle **108** possessed bright emission and supramolecular assembly behaviour [88]. Macrocyclization was accomplished by using

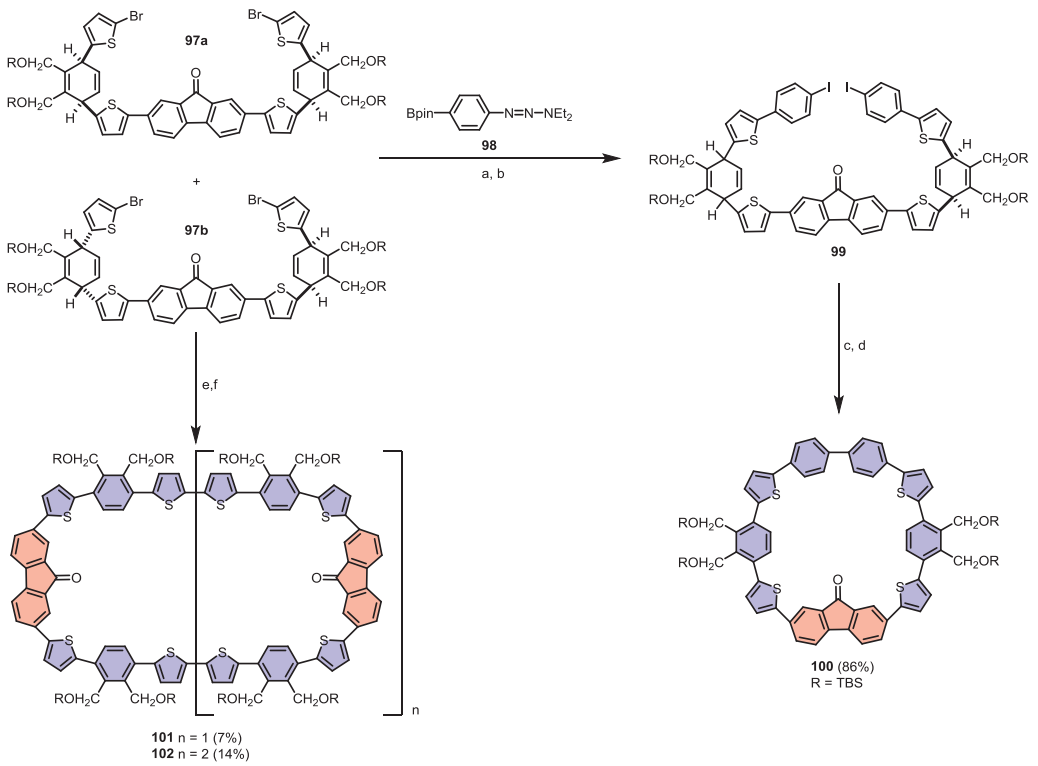

Fig. 23. Synthesis of TFOT-containing macrocycles **100**, **101** and **102**. Conditions: (a) **98**, $Pd(PPh_3)_4$, K_2CO_3, toluene/ethanol/water, 80 °C, 10 h; (b) MeI, 120 °C, 10 h; (c) $Ni(COD)_2$, bpy, THF, reflux, 24 h; (d) DDQ, 100 °C, 3 h; (e) $Ni(COD)_2$, bpy, THF, reflux, 24 h; (f) DDQ, 75 °C, 2 h. TBS = *tert*-butyldimethylsilyl, bpy = bipyridine, DDQ = 2,3-dichloro-5,6-dicyano-1,4-benzoquinone.

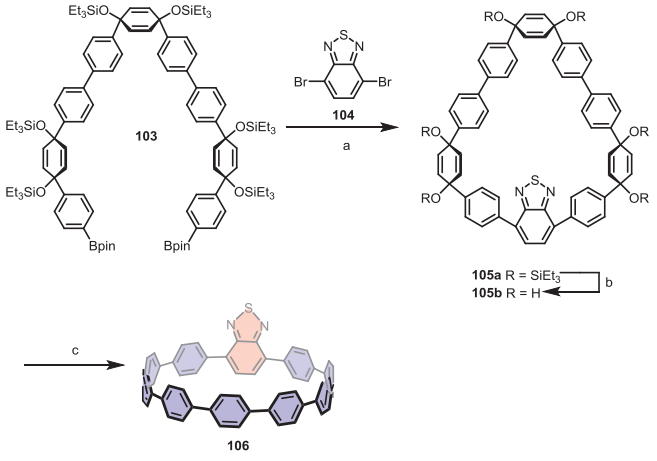

Fig. 24. Synthesis of **106**. Conditions: (a) SPhos Pd Gen III, 2 mol/L K_3PO_4, 1,4-dioxane, 80 °C, 38%; (b) TBAF, THF; (c) H_2SnCl_4, THF, 22% (2 steps).

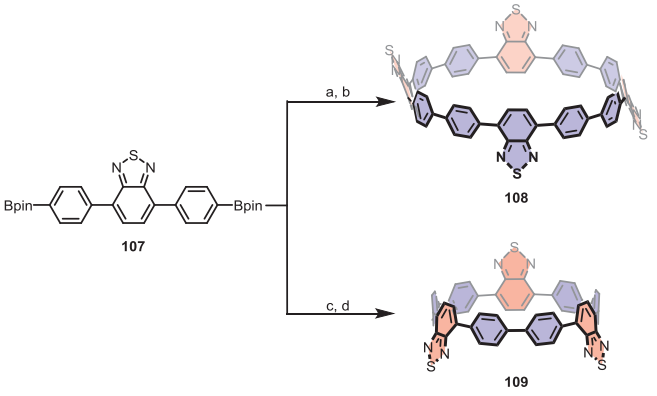

Fig. 25. Synthesis of **108** and **109**. Conditions: (a) $Pt(COD)Cl_2$, CsF, THF, reflux, 24 h; (b) PPh_3, toluene, 110 °C, 48 h; (c) $[Au_2Cl_2(dcpm)]$, Cs_2CO_3, toluene/EtOH/H_2O; (d) $PhICl_2$, DMF. Dcpm = dicyclopropylmethyl.

platinum-mediated assembly approach with *para*-borylated 4,7-diphenyl-benzothiadiazole **107**. Then a reductive elimination was taken place under the condition of PPh_3 in refluxing toluene for 48 h to afford target molecule **108** in a yield of 10%. In 2021, they further utilized the same building block **107** to fabricate macrocycle **109** with bright red emission through a gold-mediated trimerization method [89]. Macrocyclization procedure was carried out by reacting **107** with $[Au_2Cl_2(dcpm)]$ to afford a triangular cyclic intermediate. Subsequent oxidative chlorination gave the target molecule **109** with 24% isolated yield.

2.5. B/N-containing macrocycles

The tricoordinate organoboranes attract extensive attention owing to their strong electron-accepting ability. The embedding of organoboranes as A units into macrocycles would provide a mighty strategy to modulate electronic properties [90]. In 2012, the π-conjugated B-π-N macrocyclic compound **111** synthesized by Jäkle *via* organometallic condensation was firstly reported, in which the ring backbone was consisted of amine donor units and borane acceptor units linked by *para*-phenylene (Fig. 26) [91]. Reaction of linear silylated oligomer **110** with 2 equiv. of BBr_3 afforded a borylated product, then followed by treating with 4-(^{t}Bu)-*N*,*N*-bis(4-(Me_3Sn)C_6H_4) aniline under *pseudo* high-dilution conditions gave rise to the B-Br functionalized macrocyclic compound. The final B-π-N macrocycle **111** was acquired after dealing with triisopropylphene copper (TiPCu) in refluxing toluene in an overall yield of 38% after purification, in which the boron can be protected in the shield of bulky TiP groups.

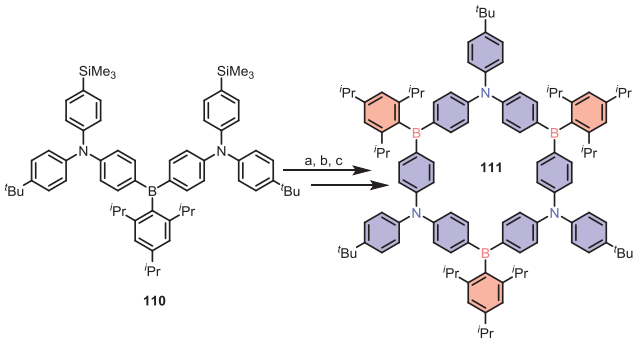

Fig. 26. Synthesis of D-π-A macrocycle **111**. Reagents: (a) BBr_3; (b) 4-(*tert*-butyl)-*N*,*N*-bis(4-(trimethylstannyl)phaenyl)aniline; (c) triisopropylphenyl copper (TipCu).

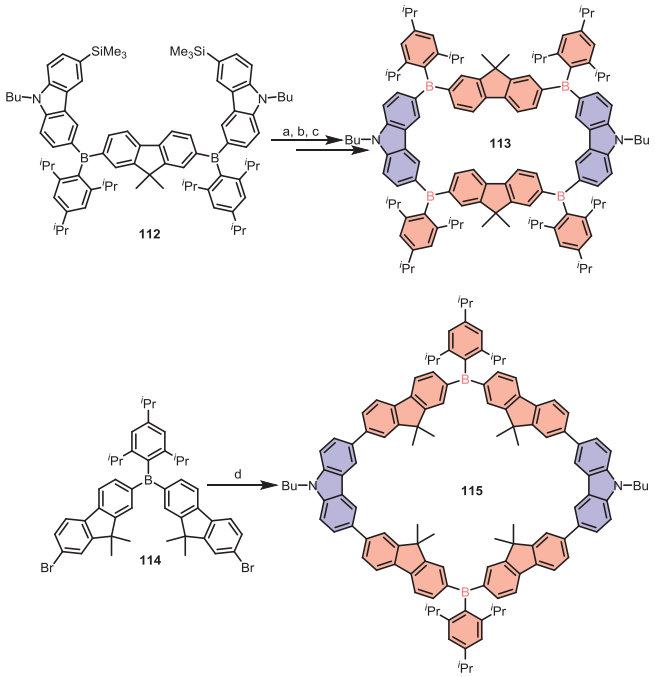

Fig. 27. Synthesis of macrocycles **113** and **115**. Conditions: (a) BBr_3; (b) 2,7-bis(trimethylstannyl)-9,9′-dimethylfluorene; (c) TipCu; (d) $Pd_2(dba)_3$, $^tBu_3P$.

In 2015, the Chen group utilized this method to further fabricate two novel unstrained B-containing macrocycles **113** and **115** employing the building blocks of 3,6-disubstituted carbazole and 2,7-disubstituted fluorene (Fig. 27) [92]. For the sake of maximizing close to the degree of endocyclic C-B-C at 120°, the DFT calculation was utilized and revealed that the skeleton of **113** comprised of two carbazole moieties and two fluorene moieties linked by four boranes and that of **115** comprised of two carbazole moieties and four fluorene moieties linked by two boranes exhibited less ring strain. The synthetic procedure of **113** was identical to that of **111** by starting with precursor **112** *via* an organometallic condensation reaction. However, macrocyclization of **115** was carried out *via* Pd-catalyzed Stille coupling under high dilution. More B-containing macrocycles with different kinds of building blocks are expected to construct *via* this modular synthetic approach.

A new D-π-A macrocycle whose skeleton is composed of fluorene and arylamine as well as organoboranes was reported by the Baser-Kirazli group [93]. The combination of organoborane and π-conjugated system endows the structure with excellent electronic characteristics owing to the electron affinity of organoboranes. As shown in Fig. 28, the precursors **116** and **117** were acquired through lithium-halogen exchange and silicon-boron exchange re-

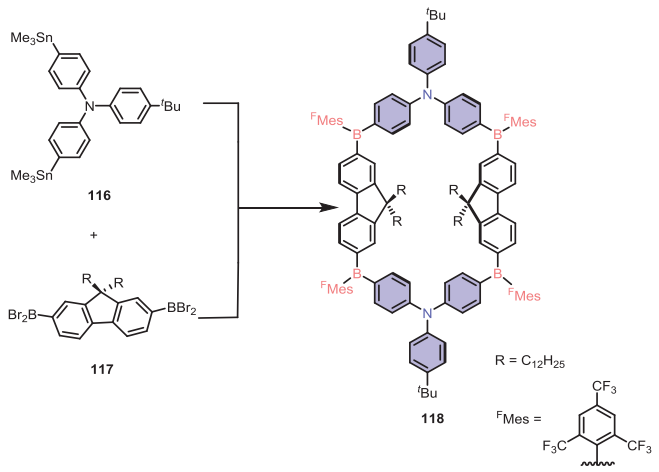

Fig. 28. Synthesis of **118**. Conditions: ^{F}MesLi, toluene, r.t.

spectively. Subsequently, organometallic condensation was performed between **116** and **117** at high-dilution conditions to access the final macrocycle **118**.

Russell and co-workers exploited Eglinton–Glaser coupling reactions in the synthesis of two macrocycles (Fig. 29) with well-defined cavities that can absorb electron-deficient C_{70} [94]. The terminal alkynes of **119** were bonded under the conditions of palladium-copper-catalyzed Eglinton–Glaser coupling, resulting in asymmetrical ring configuration **120** with a yield of 21.4%. Another macrocycle **122** with a larger diameter, was obtained through an intermolecular macrocyclization that two fragments **121** were coupled to form **122** in a yield of 8.7% with a symmetric structure. In those cyclic structures, the electron-rich triphenylamine (TPA) serve as donor units, while the electron-deficient 4,7-diphenyl-2,1,3-benzothiadiazole ($BTTh_2$) acts as acceptor units.

Pd-catalyzed Buchwald–Hartwig amination reaction was employed by Izumi and co-workers to build up an alternating D-A conjugated macrocycle **127** (Fig. 30) [95]. The double amination between dibromodibenzophenazine **124** and donor unit **123** was performed under the catalyst $Pd_2(dba)_3$ and ligand Qphos to generate **125** in a yield of 94%. After deprotected the *N*-Boc of **125** *via* TFA, macrocyclization was fulfilled by Pd-catalyzed Buchwald–Hartwig double amination of corresponding intermediate **126**, resulting in the target product **127** being obtained in with a relatively high yield of about 45%. The U-shaped dibenzo[*a*,*j*]phenazine (DBPHZ) is chosen to act as an acceptor to adjust D-A dihedral angles, while the donor part is *N*,*N*-diphenyl-*p*-phenyelendiamine, which is conducive to relieve strain and add flexibility.

In summary, three common synthetic approaches have been employed in the past years. Transition-metal-mediated coupling reactions, such as palladium-catalyzed Suzuki coupling [96], McMurry coupling between carbonyls catalyzed by $TiCl_3/LiAlH_4$ or $Zn/TiCl_4$ [97], palladium-copper-catalyzed Eglinton–Glaser coupling between terminal alkynes [66], are the common strategies used in the synthesis of DACMs. Another strategy to generate macrocyclic structures is to form a cyclic platinum complex and then experience a reductive elimination process to afford the cyclic compounds [98,99]. However, despite high efficiency, the noble metals used are the main disadvantages in these synthetic methods. The glyoxylic Pekin condensation is a potential approach to achieve DACMs with high yield owing to the dynamic covalent process.

3. Photophysical properties of DACMs

As stated above, the D-A π-conjugated macrocycles have received a great deal of attention as a result of their unique char-

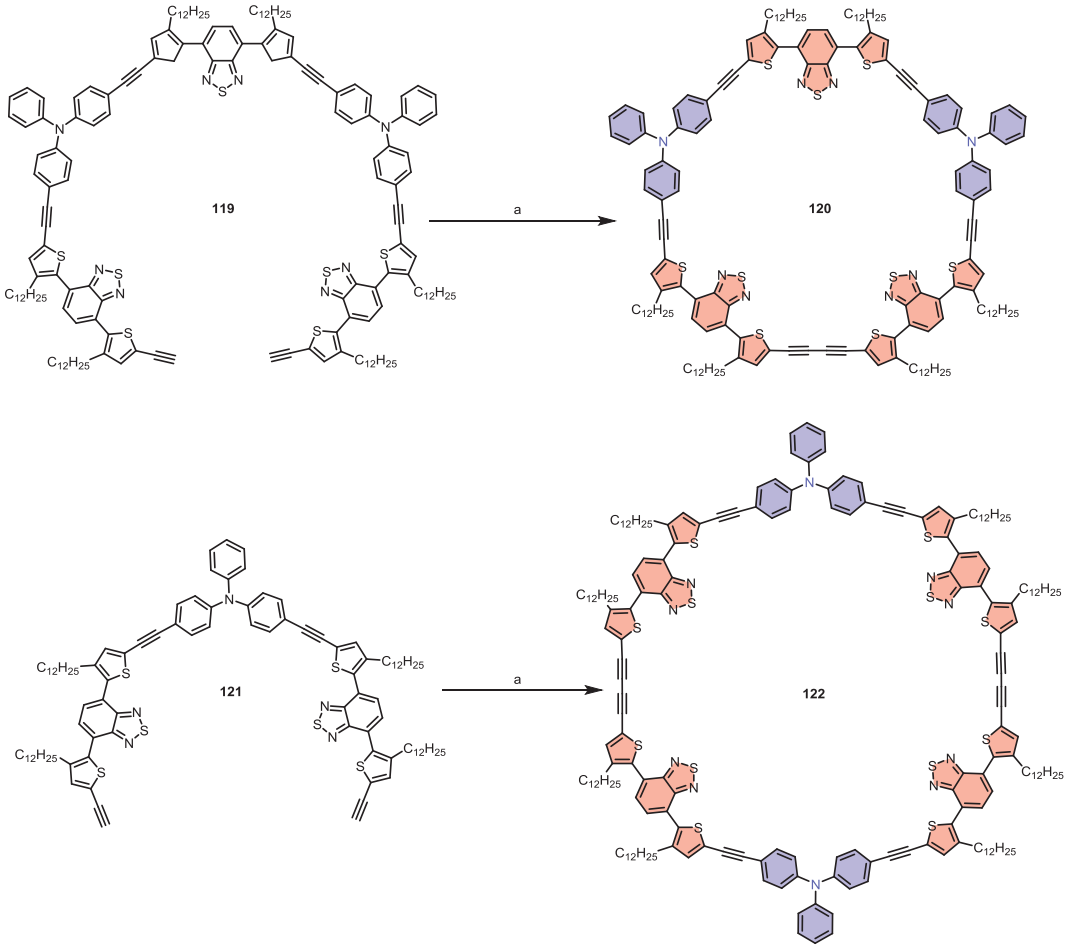

Fig. 29. Synthesis of **120** and **122**. Conditions: (a) $Pd(PPh_3)Cl_2$, CuI, $^iPr_2$-NH, r.t., 5 d.

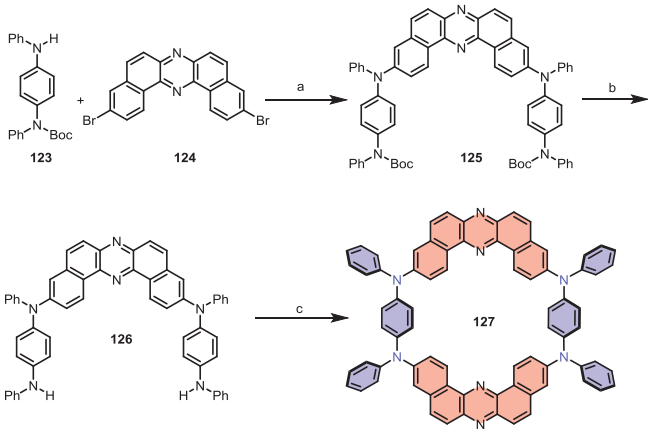

Fig. 30. Synthesis of macrocycle **127**. Conditions: (a) $Pd_2(dba)_3$, QPhos, NaO*t*-Bu, toluene, 60 °C, 12 h; (b) TFA, CH_2Cl_2, r.t., 40 min; (c) **124**, (1.0 equiv.), $Pd_2(dba)_3$, QPhos, K_2CO_3 (2.2 equiv.), 1,4-dioxane, 100 °C, 24 h. dba = dibenzylideneacetone, Qphos = 1,2,3,4,5-pentaphenyl-1′-(di-tert-butylphosphino)ferrocene.

acteristics. Understanding the relationship between structure and property is critically important for the further development of functional materials. Generally, the HOMO in conjugated molecules is determined by electron donors, while the LUMO depends on electron acceptors [100]. As a result, the energy gap of D-A π-conjugated macrocycles can be tailored by selecting appropriate building blocks with the different ability of electron affinity, thus the corresponding optical and electronic properties will be adjusted. In this regard, such a strategy holds great promise in organic optoelectronic devices. Furthermore, it is typical for D-A structures to exhibit solvatochromic luminescent properties that the polarity of solvents plays a decisive role in the emission wavelength and intensity because of charge separation in the excited state [101]. At the same time, the intramolecular charge transfer (ICT) between donor units and acceptor units can give rise to the absorption band red-shifted.

It's typical for D-A molecules to exhibit the phenomenon of solvatochromic behaviour that the emission maximum red-shifted larger with the polarity of solvents increasing, which is attributed to the separation of HOMO and LUMO in the excited states [102]. The DACMs, with spatial localization of the HOMO and LUMO, undergoes ICT upon excitation, resulting in solvatofluorochromism in non-polar solvents. When the polarity of solvents increases, non-radiative relation is more favoured in the excited stated. The incorporation of acceptor BT unit into **128** ([10]CPP) skeleton to form the D-A system remarkedly altered its optical properties. As shown in Fig. 31b, the absorption maximum of **106** was 334 nm, which was almost identical to that of parent **128** [87]. However, the emission maximum of **106** was 571 nm, which exhibited a significant Stokes shift in 237 nm and a pronounced bathochromically shifted (105 nm) compared with the parent **128** (466 nm). Interestingly, different from those acceptor-containing CPP-derivatives such as **85** with a low quantum yield (5%) account for ICT [83], **106** possessed a quantum yield up to 59% owing to the absence of ICT, which was confirmed by theoretical calculation [87]. Similarly, **108**, with four BT units incorporated into the cyclic structure, also exhibited

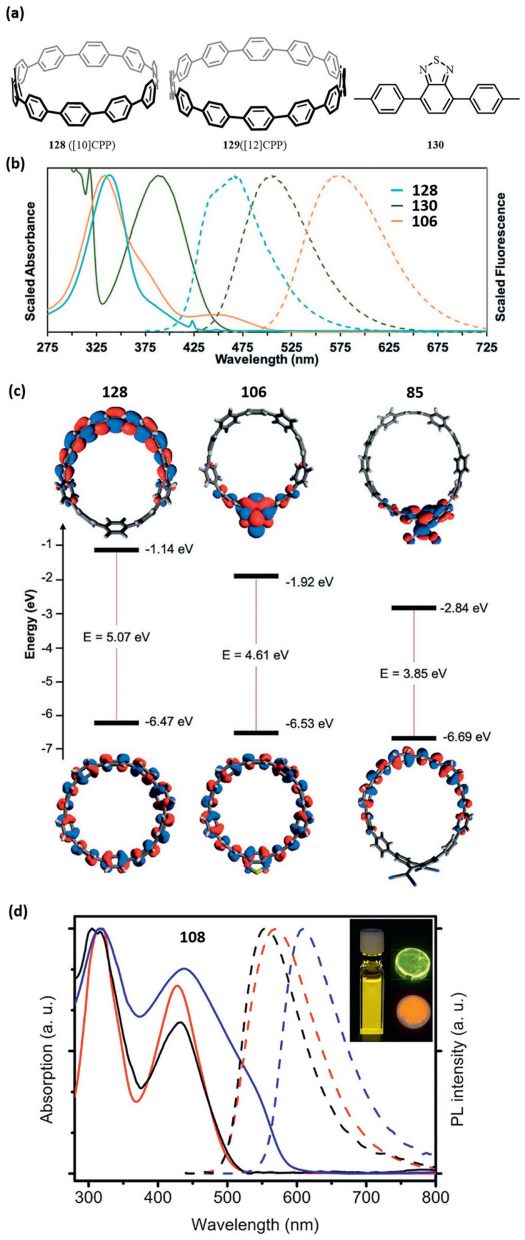

Fig. 31. (a) Structure of parent compound **128** ([10]CPP) and control compound **129** and **130**; (b) Absorption and emission spectra of **106** compared to **128** and **130** in dichloromethane; (c) The calculated frontier molecular orbitals of **128**, **106**, **85**. Reproduced with permission [87]. Copyright 2020, Wiley-VCH; (d) Absorption and emission spectra of **108** in chloroform solution (red), powder (blue), and polymethylmethacrylate film (black). Reproduced with permission [88]. Copyright 2020, Wiley-VCH.

a large red-shift emission by 119 nm in chloroform, by comparison with that of parent **128** ([12]CPP) [88]. The Stokes shift of **108** was 142 nm, which was attributed to the broken of symmetry in an excited state.

As shown in Fig. 32, the AQ-incorporated CPP molecule **84** exhibited more obvious red-shift of emission maximum when the polarity of solvents increases ($\Delta\lambda$FL max = 95 nm from carbon tetrachloride to chlorobenzene) [83]. The DFT and time-dependent DFT calculations of **84** showed that the HOMO locates at the curved oligoparaphenylene moiety while the LUMO is localized on the AQ moiety, which resulted in the solvatochromic behaviour of **84**. The HOMO-LUMO gap of acceptor-introduced **84** and **85** reduced to 2.68 eV and 1.93 eV respectively, compared with that of the parent **128** in 3.61 eV.

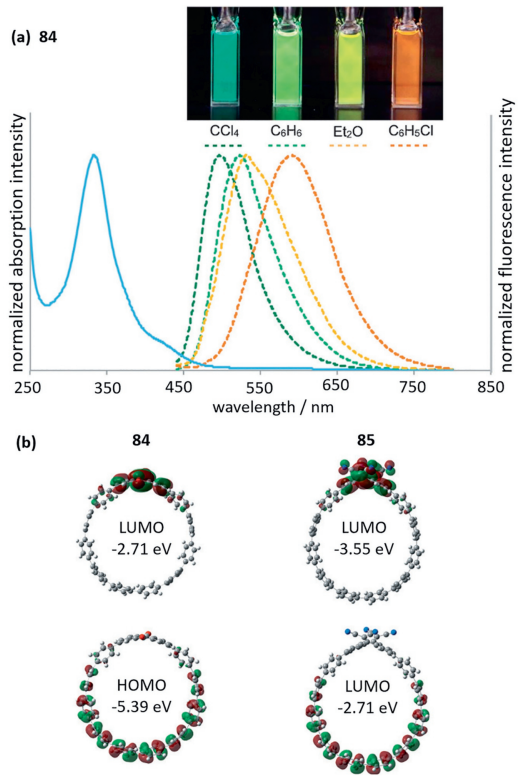

Fig. 32. (a) UV-vis absorption and fluorescence spectra of **84**; (b) HOMO and LUMO of **84** and **85** calculated at the B3LYP/6-31G(d) level. Reproduced with permission [83]. Copyright 2015, Wiley-VCH.

Similarly, the DACMs **30** and **31** also exhibited solvatochromic behaviour [53]. As shown in Fig. 33, the fluorescence spectra showed more pronounced bathochromic shifts in more polar solvents, which means charge-transfer experienced. The theoretical calculations indicated that the HOMOs are localized on veratrole moieties while the LUMOs are localized on phthalimide moieties, which accounted for the fluorescence solvatochromism. Owing to the spatial localization of the HOMO on two dialkoxyphenanthrenes moieties and 1,2-ethynylidene, and LUMO on A dibenzophenazine, a positive solvatochromism was observed in emission spectra of **37a** (Fig. 34) [69].

It is interesting that when biocompatible encapsulation agent, DSPE-mPEG$_{5000}$ was applied to produce **109** nanodots, the emission maximum of **109** nanodots redshifted to 650 nm (Fig. 35) [89]. The **109** nanodots exhibited a bright red 3PF upon excitation at 440 nm through a femtosecond laser at 1320 nm, which was confirmed to be a nonlinear optical process of 3PF *via* a power dependence relationship experiment.

Nuckolls designed and synthesized a series of cyclic and acyclic π-conjugated molecules based on diphenyl-perylenediimide (**P**) and bithiophene (**B**) to investigate the influences of macrocyclization and the D-A system toward the optical and electronic properties and performance being applied in n-type electronic materials (Fig. 36) [103]. As evidenced by absorption spectra and estimated band gap, the DACMs **47** showed a broader absorption range and narrower energy gap by contrast with that of either linear acyclic fragments **131** and **132** or cyclic compound **133** with only PDI derivatives fragments. Furthermore, the macrocyclic structures are more easily to be reduced than acyclic molecules according to cyclic voltammetry.

Based on above findings, Liu and co-workers made subtle structural modifications on conjugated macrocycle **47** with intention to understand its photophysical properties and improve its per-

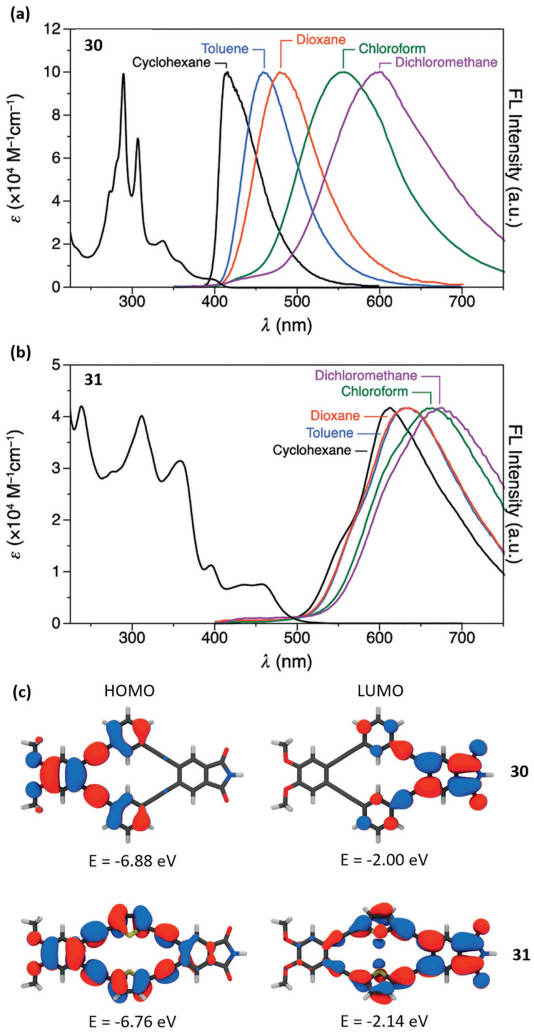

Fig. 33. UV-vis and fluorescence spectra of DACMs **30** (a) and **31** (b); (c) HOMO and LUMO of **30** and **31** calculated at the TD/PCM (cyclohexane)/CAM-B3LYP/6-311+G(2d,2p) level. Reproduced with permission [53]. Copyright 2012, American Chemical Society.

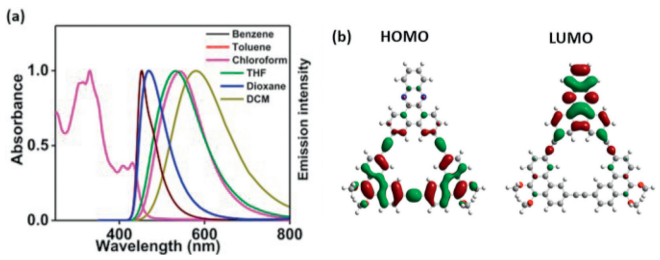

Fig. 34. (a) Normalized fluorescence spectra and (b) localization of HOMO and LUMO of **37a**. Reproduced with permission [69]. Copyright 2018, Elsevier.

formance as organic photovoltaics by theoretical calculations [73]. The time-dependent DFT functional theory was employed and revealed that when bithiophene was replaced with trithiophene or its derivatives, not only the energy gap decreased effectively but also the oscillator strengths and electron reorganization energy changed a lot, which offers a feasible way to improve the performance of DACMs to be employed as organic photovoltaics. Moreover, such subtle structural modifications on macrocycles are expected to gain higher first hyperpolarizability, which holds great prospective in second-order nonlinear optical (NLO) materials.

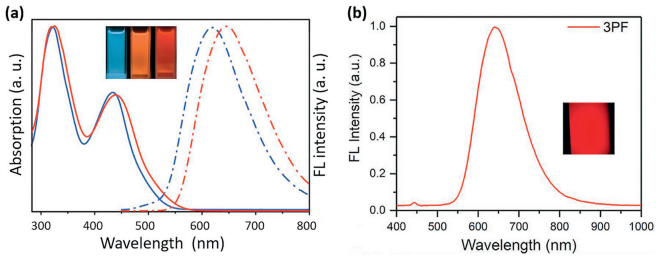

Fig. 35. (a) Absorption (solid lines) and emission spectra (dashed lines) (excitation wavelength: 434 nm) of **109** in chloroform solution (blue) and its nanodots in aqueous dispersion (red); (b) 3PF spectrum of **109** nanodots in aqueous dispersion measured under 1320 nm fs laser excitation. Reproduced with permission [89]. Copyright 2021, Wiley-VCH.

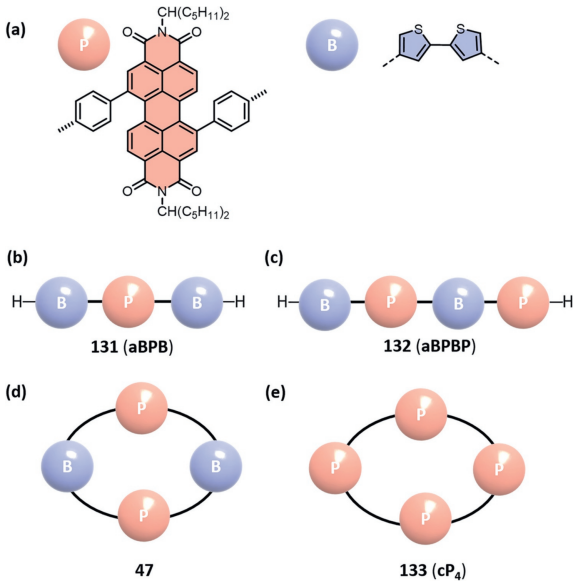

Fig. 36. (a) Schematic of diphenyl-perylenediimide denoted **P** and bithiophene denoted **B**; Acyclic structures of (b) **131** (**aBPB**) and (c) **132** (**aBPBP**); Cyclic structure of (d) **47** and (e) **133** (**cP$_4$**).

The water-soluble macrocycle **134** (WCMT-1) that comprised of two 1,6-pyrene and two phenyl units linked by four maleimides constructed by our group exhibited aggregation-induce emission (AIE) effect in low polarity solutions and the fluorescence can be quenched in aqueous solution owing to the twist intramolecular charge transfer (TICT) (Fig. 37) [104]. Interestingly, the incorporation of surfactant, sodium lauryl sulfonate (SLS), into **134** aqueous solution can keep a lid on the TICT process thus "turn on" far red/near-infrared (FR/NIR) fluorescence **134** aqueous solution.

Not only band gap can be adjusted in cyclic skeleton by incorporating variable building blocks, but the different side chains can also tune the energy gap effectively. Zahid *et al.* also designed a series of D-π-A macrocycles (**135**-**140**) (Fig. 38), in which the donor macrocycle that consisted of arylborane and 9-methylcarbazole bridged by electron-withdrawing 9,9′-dimethylfluorene performed as donors [105]. Linked by a thiophene spacer, several acceptors (**A1**-**A5**) with different electron affinity were attached to the cyclic structure and theoretical calculation was applied to explore the impacts of end-capped moieties on photoelectronic properties. The frontier molecular orbitals of these macrocycles are show in Fig. 38c, for **135**, **136**, **139** and **140**, HOMO is primarily distributed on the bridge and acceptor units and LUMO is composed of bridge and acceptor units. As for **137** and **138**, HOMO is inhibited by bridge and donor units while LUMO mainly populated by acceptor

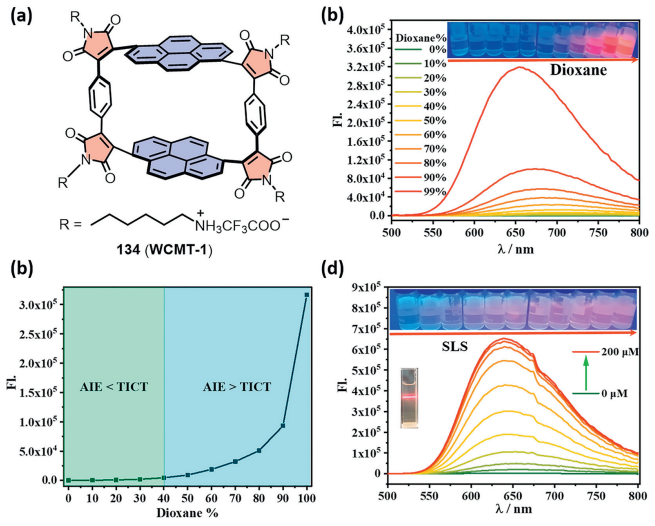

Fig. 37. (a) Structure of **134** (WCMT-1); (b) Fluorescence spectra of **134** in water with different proportion of dioxane; (c) Plot of fluorescence intensity at 650 nm *versus* Dioxane% ($C_{128} = 2.5 \times 10^{-5}$ mol/L; (d) Direct fluorescence titration of **134** in water with SLS ($\lambda_{ex} = 440$ nm). Reproduced with permission [104]. Copyright 2021, Elsevier.

and bridge units. All these macrocycles possess narrower energy gap in relation to that of **135**. The theoretical calculation results substantiated that the newly designed compounds all possessed a narrower energy gap, lower binding energy, higher dipole moment and higher charge transport abilities compared with those of the reference **135** that comprised of donor cycle with four mesityl linked at B atom. There is no doubt that such modifications have made available protocols to design functional molecules with high performance to be exploited in organic photoelectronic devices.

4. Host-guest systems of DACMs and their photophysical properties

Another peculiar property of DACMs is their well-defined cavities, which are of great importance in host-guest chemistry. These cavities can accommodate molecules with electronic activity such as electron-deficient C_{60} and C_{70}. In addition, the shape and size of guest molecules need to match up with the cavities of hosts to fix into the inner cavities. More importantly, the complexation will make a significant impact not only on the behaviour of self-assembly and the structure of host molecules to form stable host-guest systems, but also on electronic properties. For example, in 2015, Ball and co-workers developed fully conjugated chiral macrocycles by using 2,2-bithiophene (D) and (*R*/*S*-1,7-diphenyl-PDI) (A) as building blocks (Fig. 39) [72]. The novel DACMs possess well-defined elliptical cavities with a distance between two bithiophenes and two PDI is 1.0 nm and 1.6 nm, respectively. Thus, small molecules or ions could be accommodated in to the cavity, which holds a promising chance for host-guest chemistry. In 2020, they further investigated the host-guest interaction between (*R*,*R*)-**47** and fullerene C_{70} and its derivative $PC_{71}BM$ [106]. Characterization and quantification of the binding guest molecules fullerenes uncovered strong host-guest interaction with association constant (K_a) up to 9278 L/mol. A pronounced absorption and emission spectra perturbation were observed, especially the quench of (*R*,*R*)-**47** fluorescence during the process of complexation. Remarkably, the host-guest complex (*R*,*R*)-**47**/$PC_{71}BM$ outperformed macrocycle alone in electron mobility, which improved the OFET device performance more than five-fold.

In 2017, Russell group synthesized two DACMs, pentagonal **120** and hexagonal **122**, possessing cavities with diameter from 1.1 nm

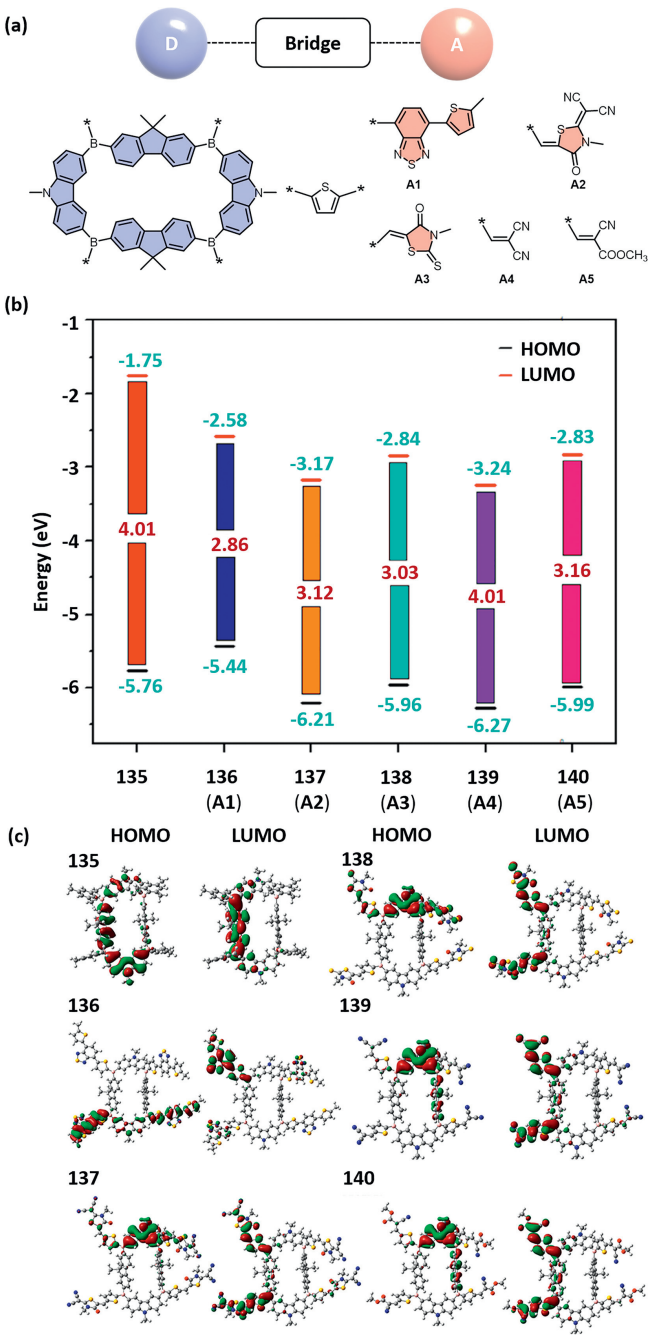

Fig. 38. (a) Sketch map of **135**-**140**; (b) Calculated HOMO and LUMO energy levels and band gaps of **135**-**140**; (c) HOMO and LUMO of **135**-**140**. Reproduced with permission [105]. Copyright 2021, American Chemical Society.

to 1.8 nm and 1.8 nm to 2.6 nm respectively, in which the ring skeletons are comprised of TPA and $BTTh_2$ linked by acetylene (Fig. 40) [94]. In the cyclic skeleton, the TPA is functioned as electron-donor, while $BTTh_2$ serves as electron-acceptor. Given the suitable electronic structure and large cavity of the macrocycles **120** and **122** respectively, the formation of host-guest systems with electronically active molecules are expected. Electron-deficient C_{60} and C_{70} or its derivative $PC_{71}BM$ can be incorporated into the cavity of **120** with the ratio of 1:1 to form host-guest complex, while one **122** molecular can accommodate two C_{70} in its inner cavity. Interestingly, the C_{70} was existed in the side of the cavity near $BTTh_2$ instead of the central location, which is ascribed to the S···π interaction that can stabilize the **120**⊃C_{70} complex. Fluorescence

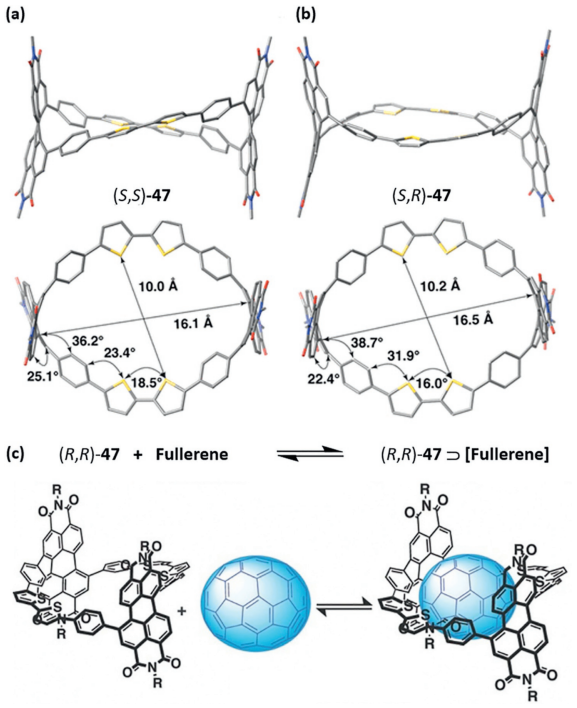

Fig. 39. DFT-minimized model (side-on and face-on views) of stereoisomer (a) (*S*,*S*)-**47**; (b) (*R*,*S*)-**47**. Reproduced with permission [72]. Copyright 2015, American Chemical Society; (c) (*R*,*R*)-**47**⊃$PC_{71}BM$ complex. Reproduced with permission [106]. Copyright 2020, Wiley-VCH.

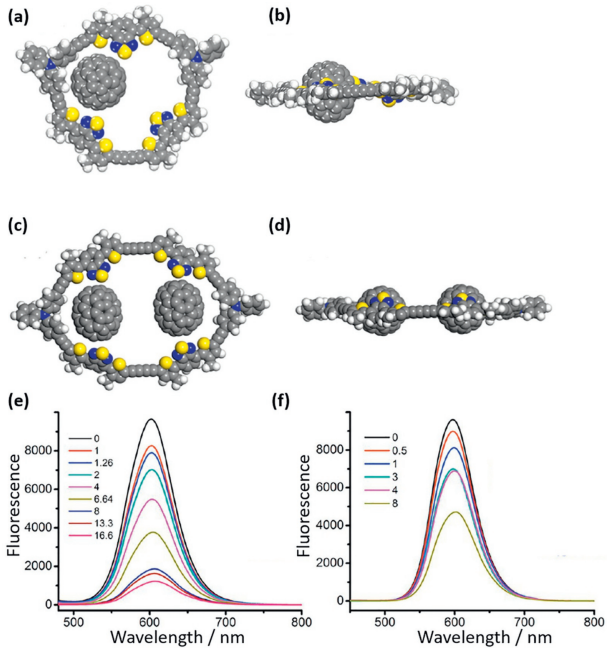

Fig. 40. Energy-minimized geometry for complexes of (a, b) **120**⊃C_{70}; (c, d) **122**⊃C70 (gray: C; blue: sulfur; yellow: nitrogen); Fluorescence titration of (e) **120** and (f) **122** with C_{70}. Reproduced with permission [94]. Copyright 2017, American Chemical Society.

titration of **120** and **122** with C_{70} exhibited an obvious quench of fluorescence intensity and the association constants were calculated to be 1.95×10^4 L/mol for **120**⊃$2C_{60}$ and 1.33×10^4 L/mol for **122**⊃$2C_{60}$, which was in accordance with the results that the complexation between **120** or**122** and C_{60} exists. The blended film made by complex of **120**⊃$PC_{71}BM$ for organic solar cell afforded a

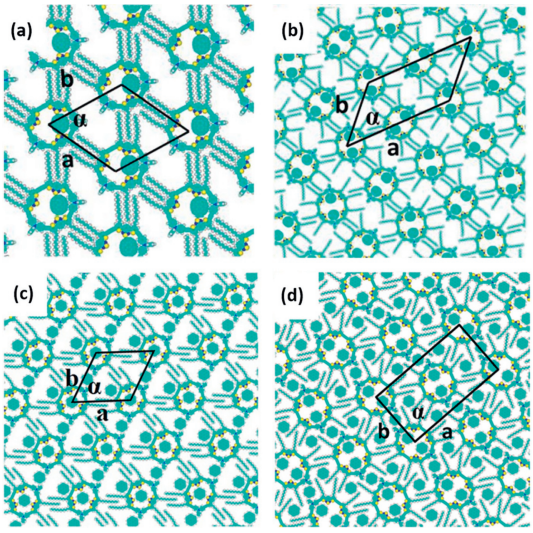

Fig. 41. DFT calculated models of (a) **120**⊃C_{70}; (b) **122**⊃C_{70}; (c)**120**⊃COR; (d) **122**⊃COR. Reproduced with permission [107]. Copyright 2018, Elsevier.

significant power conversion efficiency, which can be considered as functional materials for photovoltaic application.

In 2018, based on the above discovery, Cheng and co-workers further researched what differences will make if the guest molecular, coronene (COR), was added into the host-guest systems formed by complexes **120**⊃C_{70} and **122**⊃C_{70} (Fig. 41) [107]. When processed at the 1-phenyloctane/HOPG interface, both of macrocycles **120** and **122** exhibit different self-assembled patterns at different concentrations according to the scanning tunneling microscopy. At low concentration, the monomeric **120**⊃C_{70} complexes direct the same position. However, as the concentration increases slowly, the **120**⊃C_{70} complexes tend to exhibit dimerized and turn to zigzag patterns. Once COR solution is added into the **120**⊃C_{70} system, the arrangement patterns mentioned before are gone, replaced by a loose packing model. As shown in picture 41, not only inside the cavity is a guest COR molecular, but near the cycle skeleton and adjacent macrocycles still exist COR molecules on account of adsorption and π conjugation. As a result, the host-guest system of **120**⊃COR emerged with a ratio of 1:3 (**120**:COR). Similarly, there are two guest COR incorporated into the cavity of **122**. Interestingly, the hole formed by long alkyl chains of adjacent **122** can accommodate guest molecules as well, thereby resulted in a host-guest network in a ratio of 1:5 (**122**:COR). Obviously, macrocycles/COR complexes are more stable than macrocycles/C_{70}. The DFT calculation indicates that the macrocycles/COR benefit more in thermodynamics. At the meantime, the planarity and π-conjugated structure of COR play a crucial role in stabilizing macrocycles/COR complexes, which can form strong π-π interactions with the HOPG interface.

The macrocycle **7** with intrinsic inner cavity also possesses great potential in binging small guest molecules [60]. As evidenced by sing-crystal X-ray diffraction (Fig. 42), one *p*-xylene molecule trapped into the cavity of macrocycle **7** when methanol was slowly diffused into a *p*-xylene solution of **7** to get its single crystal. Therefore, more stable host-guest system is anticipated to attain if suitable guest molecules are found.

Owing to the large skeleton of **106**, C_{60} can be absorbed into its inner cavity [87]. As shown in Fig. 43b, the host-guest interaction between **106** and C_{60} led to a completely quench of fluorescence the fluorescence was quenched. A high binding constant, *ca.* 2.06×10^4 L/mol was obtained.

Benefiting from the large size of **108**, the supramolecular assembly of **108** with fullerene was also investigated [88]. Besides,

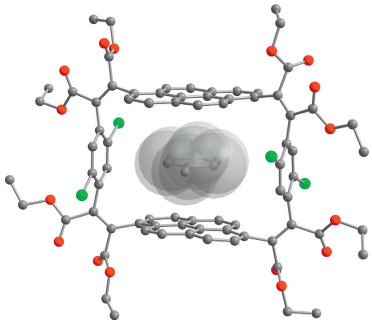

Fig. 42. Crystal structure of macrocycle **7**, inside the cavity is a *p*-xylene molecule (gray: C; green: Br; red: O).

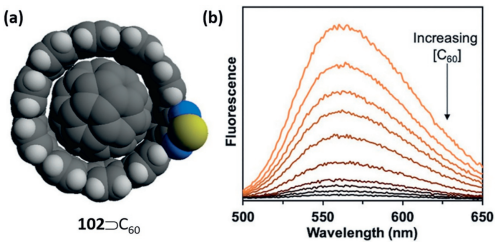

Fig. 43. (a) **106**⊃C_{60}; (b) **106** fluorescence quenching by C_{60}. Reproduced with permission [87]. Copyright 2020, Wiley-VCH.

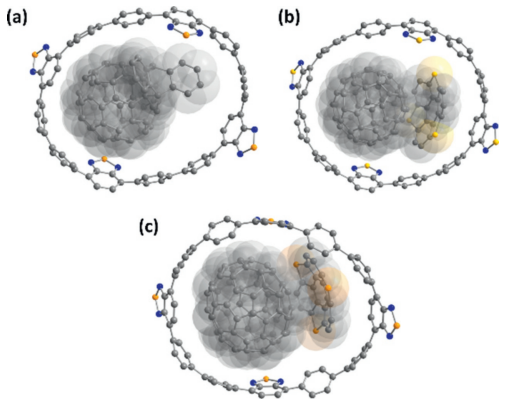

Fig. 44. Structure of the supramolecular assemblies of **108**. (a) Anthracene-C_{60}@**108**; (b) trithiasumanene⊃C_{60}@**104**; (c) (trithiasumanene)⊃C_{70}@**108** (gray: C; blue: sulfur; yellow: nitrogen).

the incorporation of the guest molecules also exerted a great influence on the conformation of host compound. As evidenced by single crystal X-ray diffraction, the average diameter of the inner cavity of **108** reached up to 16.5 Å, which was enough to accommodate large host molecules. Interestingly, when assembled with anthracene-C_{60}, **108** underwent a deformation into elliptical conformation with long and short axis of 17.8 and 14.7 Å, respectively, as shown in Fig. 44a. The self-assembly of anthracene-C_{60}@**108** was stabilized by $\pi\cdots\pi$ interactions of fullerene and CH$\cdots\pi$ interactions of anthracene and the binding constant was determined to be *ca.* 1.87×10^4 L/mol calculated by fluorescence titration. Ternary cocrystallization of **108**, C_{60}/C_{70} and trithiasumanene were also performed. The hoop of **108** transformed into an oval shaped structure in the supramolecular assembly of (trithiasumanene⊃C_{70})@**108** due to the larger size of C_{70}. As a result, **108** can serve as an adaptive host that the structure of macrocycle **108** can adjust its conformation according to different guest molecules.

5. Applications of DACMs

5.1. Chemical sensors

The incorporation of heteroatom into macrocycles is a useful tool to furnish macrocycles with different functions. In 2004, the dehydroannulene-type cyclophane **15** developed by Baxter possessed a special ability of coordination toward certain metal ions, in which the cyclic structure encompassed donor thiophene and acceptor pyridine units linked by ethynylene [67]. It was found that a yellow precipitate emerged when **15** and AgCl were mixed in 10% MeOH/$CHCl_3$ in five minutes. However, the precipitate disappeared completely when a saturated 10% H_2O/MeOH solution of KCN was added, which confirmed the coordination is a reversible process. Moreover, a bright orange luminescence was observed in the precipitate of **15**/AgI. By contrast, a visually pronounced fluorescence quenching occurred in the solution of **15**/NiII. The special phenomenon of chromogenic fluorescence and precipitate of **15** toward AgI provide a platform for **15** to be utilized as AgI sensors. Additionally, the D-A conjugated macrocycle **15** holds great promise in applying for NiII sensors in biological media owing to the fluorescence quenching/precipitate caused by NiII.

Recently, our group prepared a DACMs **141** comprising of 1,6-pyrenylene and 1,4-phenylene linked by maleimides, which exhibited vapochromic behavior [52]. Two crystals with different colours, the yellow crystallite **141*α*** and the red crystallite **141*β*** (Fig. 45c), were obtained *via* different crystal growth methods. The frontier orbitals were separated that HOMO is occupied by pyrene moiety and LUMO is mainly distributed on the maleimide and benzene units, which indicated the D-A character of **141**. Interestingly, when exposed to saturated vapour of volatile solvents such as dichloromethane, tetrahydrofuran and toluene overnight, the yellow crystallite **141*α*** transferred into the red crystallite **141*β*** along with the changes of conformation (Fig. 45d), which have been sustained by powder X-ray diffraction (PXRD). This conversion was attributed to the flip of pyrene induced by the vapor of solvent and was an irreversible process, which creates the possibility of being applied for environmental management and industrial monitoring.

5.2. Bioimaging

Organic materials with near-infrared (NIR) fluorescence hold great potential in the field of bioimaging [108,109]. In order to extend their emissions to NIR region, the common strategies are the introduction of strong electron-donating and electron-accepting units or scale-up of π-conjugation [110]. In this regard, DACMs are anticipated to enter this field. In 2021, our group constructed a water-soluble DAMC, namely **134**, in which the main backbone comprised of 1,6-position pyrenes and 1,4-position benzenes linked by four maleimides (Fig. 46) [104]. Interestingly, the incorporation of surfactant, sodium lauryl sulfonate (SLS), into **134** can keep a lid on TICT process thus "turn on" far-red/near-infrared (FR/NIR) fluorescence in **134** aqueous solution. Further analysis of controlled experiments shed light on both electrostatic and hydrophobic interactions are critically important in creating supra-amphiphile for this switch. Hela and HepG2 cancer cells were chosen to carry out bioimaging experiments. It is found out that the two types of cells were capable of fluorescent response when deal with SLS and **134**. Meanwhile, the existence of **134**&SLS has no impact on cell viability.

The above results provide us with reference and guidance for subsequent molecular design. To address the issue of lacking specificity, triphenylphosphonium cation (TPP) was integrated into four maleimides and the skeleton of macrocyclic structure remains the same (Fig. 47) [111]. The novel designed compound, **142**, can achieve a 650+ nm emission and large Stokes shift of about

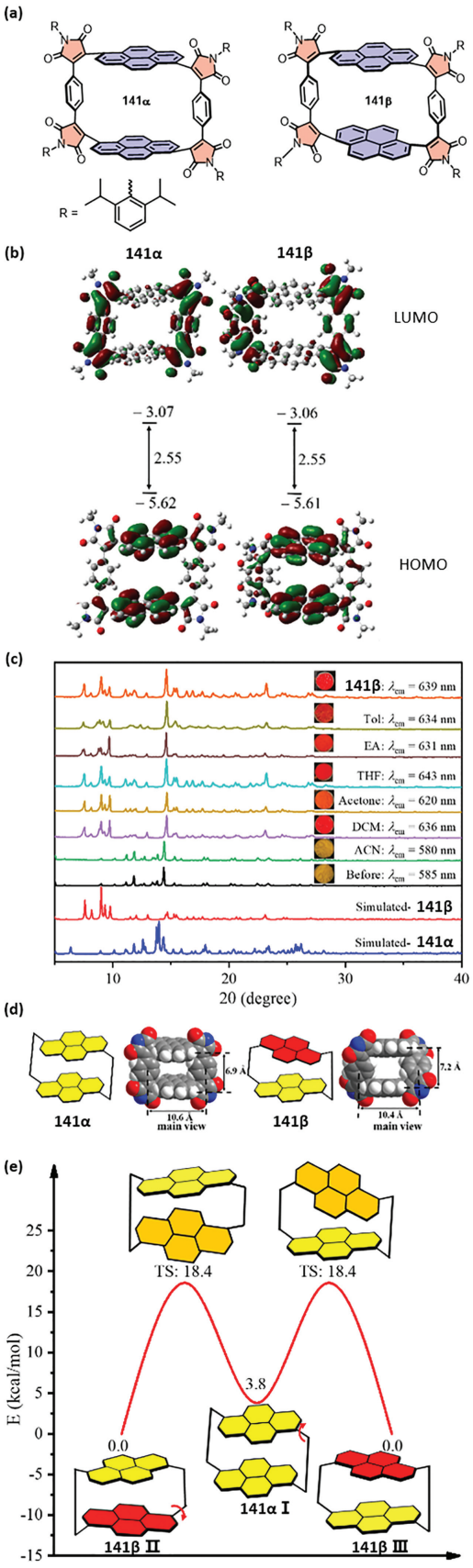

Fig. 45. (a) Structure of **141**; (b) The frontier orbitals of **141*α*** and **141*β***; (c) The PXRD and the photographs of **141*α*** before and after adsorption different solvents; (d) The model and main view in the space-filling model of **141*α*** and **141*β***; (e) The interconversion process between **141*α*** and **141*β*** and related thermal free energies. Reproduced with permission [52]. Copyright 2021, Elsevier.

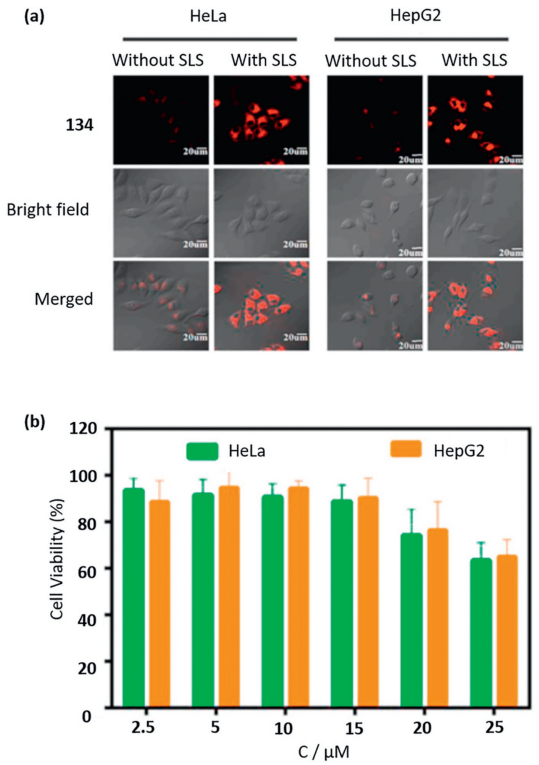

Fig. 46. (a) Confocal fluorescence images of HeLa cells and HepG2 cells pretreated with or without SLS (30 μmol/L) and then incubated with **134** (10 μmol/L); (b) Cell viability of HeLa cells and HepG2 cells treated with different concentrations of **134**&SLS (1:3) supra-amphiphile. Reproduced with permission [104]. Copyright 2021, ELSEVIER.

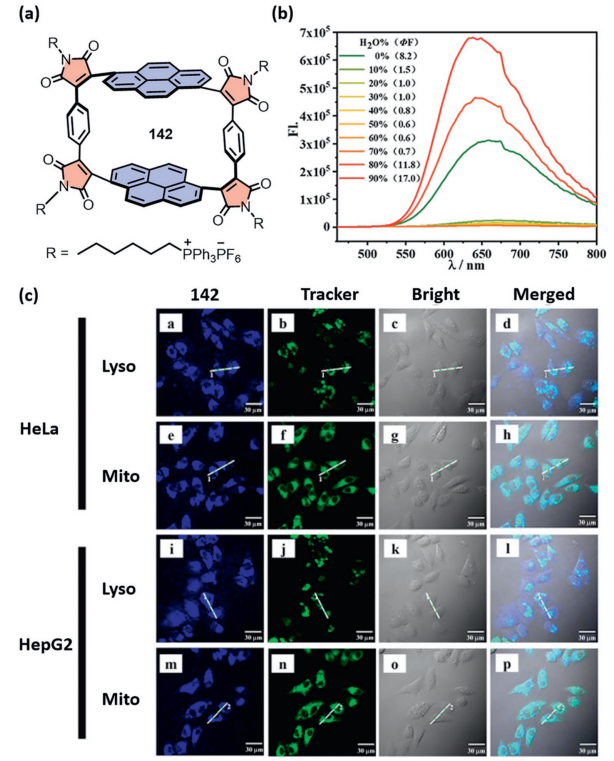

Fig. 47. (a) Structure of **142**; (b) Fluorescence spectra of **142** in acetonitrile/water mixed solvent; (c) Subcellular localization experiments in living HeLa and HepG2 cells. Reproduced with permission [111]. Copyright 2021, WILEY-VCH.

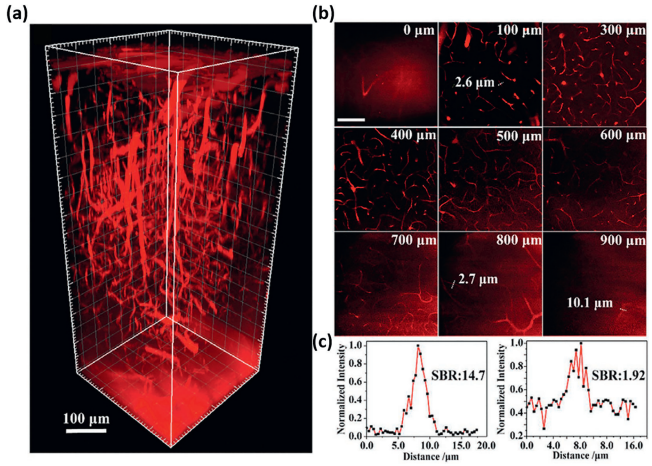

Fig. 48. (a) 3D reconstruction of the vasculature (0–900 μm); (b) 3PF cerebrovascular imaging at various vertical depths, scale bar = 100 μm; (c) SBR ratio analysis of blood vessels at 100 (left) and 800 μm (right), excitation: 1320 nm fs laser (1 MHz). Reproduce with permission [89]. Copyright 2021, Wiley-VCH.

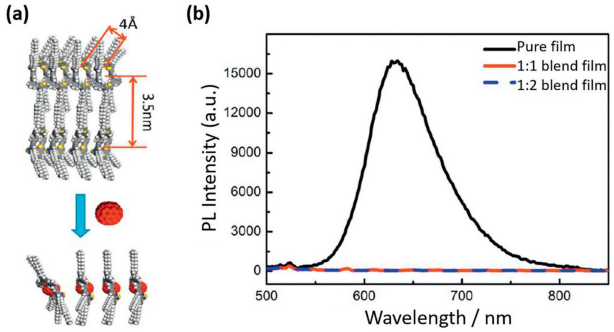

Fig. 49. (a) Suggested molecular models of the assembly structures for **120** before and after adding $PC_{71}BM$; (b) Photoluminescence spectra. Reproduced with permission [94]. Copyright 2017, American Chemical Society.

200+ nm, which is expected to offer new opportunities in the field of FR/NIR bioimaging. The AIE effect is discovered when the ratio of water in the mixed solvent is more than 80%, for which the solubility of **142** is worse in an aqueous solution than that in organic solvents. Meanwhile, the addition of SLS to **142** aqueous solutions can further enhance fluorescence owing to the electrostatic interaction. More importantly, the distributed synchronicity of fluorescence intensity between Mito-Tracker Green FM and **142** as well as high biocompatibility of Hela or HepG2 and make TPP-CMT a promising candidate in the field of mitochondrial-targeting bioimaging.

The macrocycle **109**, with red emission and unique three-photon fluorescence (3PF) characteristic, exhibited promising prospective in fluorescence cerebrovascular imaging [112]. As shown in Fig. 48, the imaging of mouse cerebrovascular exhibited a clear contrast owing to its bright emission. A higher signal-to-background ratio (SBR), 14.7 in 2.6 μm blood vessel at imaging depth of 100 μm was observed in comparison to that of (1.92) in 2.7 μm vessel at imaging depth of 800 μm. Also, the penetration depth can even reach up to 900 μm.

5.3. Photoelectronic devices

5.3.1. Organic photovoltaics (OPVs)

The energy gap of DACMs can be tailored effectively by introducing appropriate D and A units into macrocyclic backbones, resulting in modular optical properties and electronic structures. Moreover, DACMs with controllable structures can align into ordered 2D and 3D self-assembly that are conducive to charge transfer. Additionally, introducing different building blocks into cyclic skeletons equip macrocycles with desired functions that broaden their applications as functional materials. For example, thiophene is a common building block to construct functional materials in organic electronic devices as a result of its high stability and polarizability as well as outstanding charge transport ability [113,114]. Cooke reported a thiophene-based macrocycle to be applied in organic field-effect transistors (OFETs) [71].

In 2016, Ball and co-workers compared the performance of the macrocycles **47** and their corresponding acyclic analogues **131** and **132** whose basic structural units were bithiophene and diphenylperylenediimide in organic optovoltaics for the first time [103]. The X-ray crystallographic and spectra analyses, as well as DFT calculations of these macrocyclic structures and corresponding acyclic fragments revealed the importance of molecular structure and supramolecular self-assembly in enhancing the performance of optovoltaic and optoelectronic materials. The UV-vis spectra exhibited larger absorption range of cyclic structures with respect to acyclic counterparts. The electron mobility was estimated by fabricating thin-film semiconductors and the results indicated that cyclic molecules **47** and **133** exhibited a pronounced advantage than acyclic analogues **132** and **132**. Further analysis of atomic force microscopy displayed cyclic molecules showed greater potential in bulk heterojunction (BHJ) solar cells. The overall excellent properties endow the cyclic structures with higher power conversion efficiency (PCE) than that of acyclic analogues. This investigation sheds light on the importance of geometry toward the performance of optovoltaic devices and make it a promising modular method for electron transport materials.

The DACMs **120** and **122** consisting of TPA and $BTTh_2$ were synthesized by Zhang and co-workers [94]. Taking advantage of their large cavities that absorb guest molecules, host-guest complexes with C_{70} or $PC_{71}BM$ were successfully constructed. The **120**, serving as electron donor material, was blended with $PC_{71}BM$ to fabricate BHJ organic solar cells (OSCs). Different ratios of D/A weight (form 1:1 to 1:4) were investigated and the results exhibited the highest PCE in 2.66% with the ratio of 1:3 while **122** in the 1:4 blend with $PC_{71}BM$ obtained highest PCE of 1.28%. Adding $PC_{71}BM$ to pristine film of **120** resulted in entirely quench of fluorescence, which indicates the electron transfer from D unit **120** to A unit $PC_{71}BM$ with high efficiency (Fig. 49). To this end, such host-guest systems provide excellent opportunities for fabricating OSCs. Remarkably, the ratio of conjugated macrocycle donor and fullerene acceptor has great impacts on the PCE of the device. This work makes D-A macrocycles available for fabricating OSCs with fullerene acceptor and offers a promising direction for optimizing the performance of OSC.

In 2018, Li *et al.* reported on the first synthesis of a diketopyrrolopyrrole (DPP) based D-A macrocycle, in which the cyclic backbone linked electron-deficient DPP and electron-rich bithiophene in an alternating D-A-D-A pattern [54]. The broad emission ranging from 700 nm to 1000 nm enables **69** to be utilized in near-infrared OLEDs. Interestingly, **69** exhibited amorphous morphology in thin film but can still possess good ability of charge transporting. When **69** was applied as non-fullerene acceptors in OSCs, a PCE of 0.49% was obtained, which was in direct contrast to that of linear analogue in 0.03% PCE. dos Santos and co-workers achieved two macrocyclic structures based on thiophene moiety **143** and **45**, which can perform as donors to be applied in OSCs [71]. Four benzothiadiazole (BT) units was introduced into the skeleton of **143** to form the macrocycle **45** with a D-A system. As shown in Fig. 50c, the HOMO and LUMO electron density distribution of **143** are almost overlapped in the whole skeleton. However, **45** exhibited D-A character that LUMO is primarily populated by the BT units. The

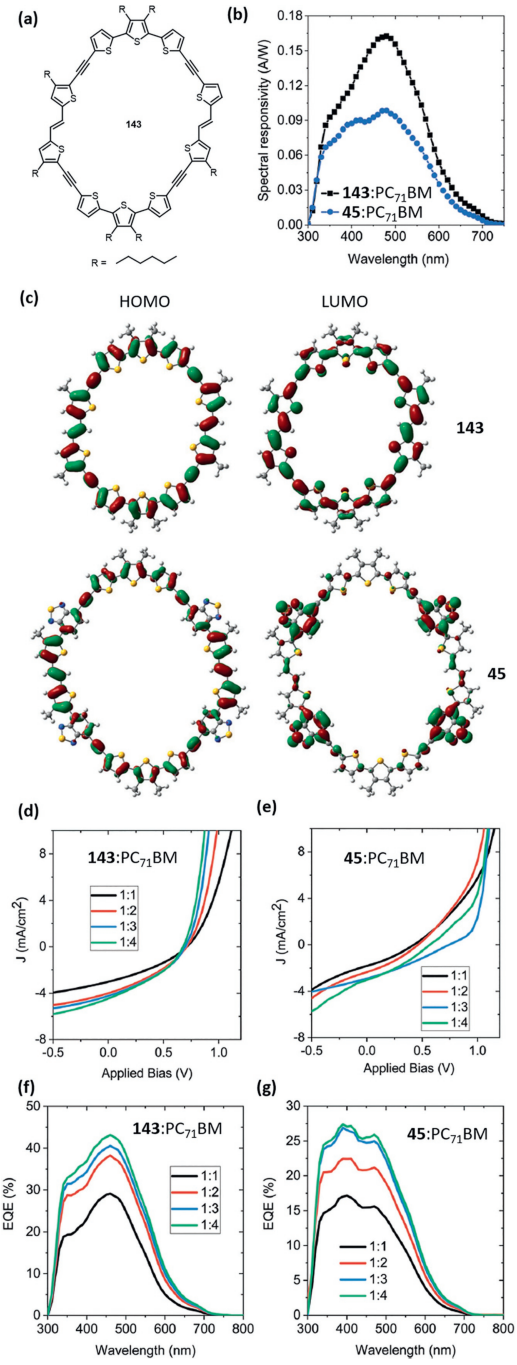

Fig. 50. (a) Structure of **143**; (b) Spectral responsivity curves of the corresponding photovoltaic devices estimated from their EQE spectra; (c) HOMO and LUMO of **143** and **45**; *J-V* characteristics of the (d) **143**: $PC_{71}BM$ and (e) **45**: $PC_{71}BM$ blends; External quantum efficiency (EQE) spectra of the (f) **143**: $PC_{71}BM$ and (g) **45**: $PC_{71}BM$ blends. Reproduced with permission [71]. Copyright 2021, The Royal Society of Chemistry.

maximum absorption of **45** red-shifted in comparison with that of **143**, which stemmed from the ICT effect of the D-A system. The cyclic voltammetry (CV) revealed that the two molecules can be served as donor materials, which was confirmed by DFT calculation. As a result, $PC_{71}BM$ was selected as acceptor to fabricated OSCs with the two macrocycles. The devices obtained PCEs of 1.1% for **143** and 0.63% for **45** (Fig. 50). Such poor PCEs were attributed to narrow absorption. However, it provides access to be applied in photodetectors with the external quantum efficiency (EQE) of 40% for **143** and 25% for **45**.

5.3.2. Organic light-emitting diodes (OLEDs)

Since the special phenomena, thermally activated delayed fluorescence (TADF) was first exploited in OLEDs by Endo *et al.*, it has attracted extensive attention [115]. Compared to traditionally luminous and phosphorescent OLED materials, TADF materials are a class of highly efficient OLED emitters. Triplet excitons can transfer to singlet excitons through thermally conversion by a fast reverse intersystem crossing (RISC) process. Thus, the energy gap of highly efficient TADF emitters between singlet and triplet must be as small as possible [116,117]. The strategy of incorporating D units and A units can exactly meet this requirement. Conjugated macrocycles with D-A system can separate HOMO and LUMO in space, which is conducive to get a small bandgap.

In 2020, Izumi *et al.* developed a D-A-D-A conjugated macrocycle by employing two U-shaped *N,N*-diphenyl-*p*-phenyelendiamine as donor units and dibenzo[*a,j*]phenazine (DBPHZ) as acceptor units [95]. Given the fact that DBPHZ plays a significant role in narrowing energy gap and its U-shaped structure, it is a suitable building block to construct a macrocyclic structure for TADF materials. In order to gain insights into the impact of cyclization on photophysical and redox properties, the author synthesized a linear molecule **144** and cyclic structure **127** for comparison. The emission of linear analogue exhibited a larger red-shifted than that of **127**, which is ascribed to the free rotation of the D-A system. As shown in Fig. 51b, the HOMO of **127** is localized on the whole ring while the LUMO is mainly inhibited by A units DBPHZ. As for **144**, the electron density in the HOMO and LUMO was primarily occupied by D and A, respectively. Theoretical analysis of time-resolved luminescence spectroscopy indicated that the macrocycle **127** possesses a greater advantage in both RISC process and delayed fluorescence contribution than linear analogue counterpart. As evidenced by the fabrication and characteristics of OLED emitters, the cyclization afforded the conjugated macrocycle **127** for higher efficient TADF property, whose external quantum efficiency (EQE) reached up to 11.6% (Fig. 51) when served as an OLED emitter while that of linear oligomer **144** was 6.9%. It is a prominent progress that the EQE of the twisted D-A conjugated macrocycle is far beyond conventional fluorescent materials.

Shikita *et al.* also demonstrated that cyclic configuration possessed a superior performance when served as an OLED emitter than the acyclic counterpart [81]. As shown in Fig. 52b, the HOMO of DACMs **79** is populated by three carbazole units and the LUMO is inhibited by entire macrocyclic skeleton, which is different from that of **145** with LUMO distributed on the central triazine and adjacent phenylene rings. The macrocyclic compound **79**, with a low S_1-T_1 energy gap (0.14 eV) determined by experiment, possessed the TADF ability while the linear molecule **145** did not. When fabricated as OLED emitters, the **79**-based device exhibited a 4-fold increase in electroluminescence efficiency than that of acyclic analogue **145**.

5.3.3. Organic fields effect transistor (OFET)

The electron mobility is an important parameter in OFET devices for which low carrier mobility is unfavourable for carrier extraction. Two different D-A conjugated macrocyclic conformation, *trans*-**52** and *cis*-**50**, composing of chiral, helical perylene diimide ribbons and bithiophene were achieved by Ball and coworkers (Fig. 53) [75]. The LUMO determined by cyclic voltammetry was estimated to be –3.80 eV for *trans*-**52** and –3.82 eV for *cis*-**50**, which are similar to the parent helical perylene diimide and anticipated to perform as n-type semiconductors. Pronounced discrepancy of the two molecular conformations was observed. The *cis*-**50** presented a "tent" shape with less strain and more flexibility, whereas the *trans*-**52** showed an "upright" with more rigidity, leading to a 4-fold increase in electron mobility of *cis*-**50** by contrast with that of *trans*-**52**.

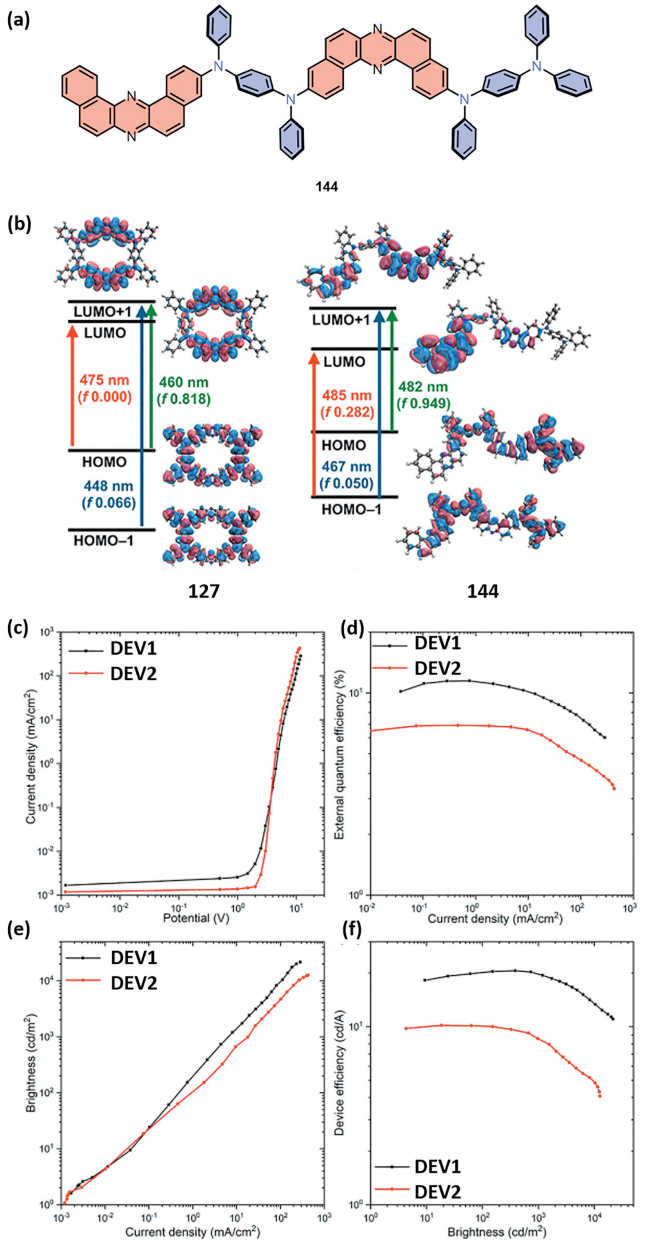

Fig. 51. (a) Structure of linear analogue **144**; (b) Energy-level and frontier molecular orbitals of **127** and **144**; (c-f) OLED device characteristics fabricated with macrocycle **127** (DEV_1) and corresponding linear oligomer **144** (DEV_2). Reproduced with permission [95]. Copyright 2020, American Chemical Society.

The strong interaction between (*R*,*R*)-**47** and $PC_{61}BM$ exert a pronounced improvement on the performance of OFET device [106]. When (*R*,*R*)-**47**⊃$PC_{61}BM$ was fabricated into thin films in the active layer (Fig. 54), the electron mobility increased more than five-fold compared with that of (*R*,*R*)-**47**. The DACMs **69**, with amorphous morphology in film, also exhibited good charge transport ability by OFET measurements [54]. These investigations show that DACMs possess great potential application in OFET.

Functionalization also offers a feasible strategy to broaden the applications of D-A macrocycles. As shown in Fig. 55a, functionalization with bromine atoms in thiophene rings facilitate **48**-Br_{12} self-assembly, thus a three-dimensional capsular structure was obtained in the solid state and in films [74]. The blended film made by **48**-Br_{12} exhibited electron mobility more than 20-folds by contrast with that of **48**. The cellular films in OFET active layer pos-

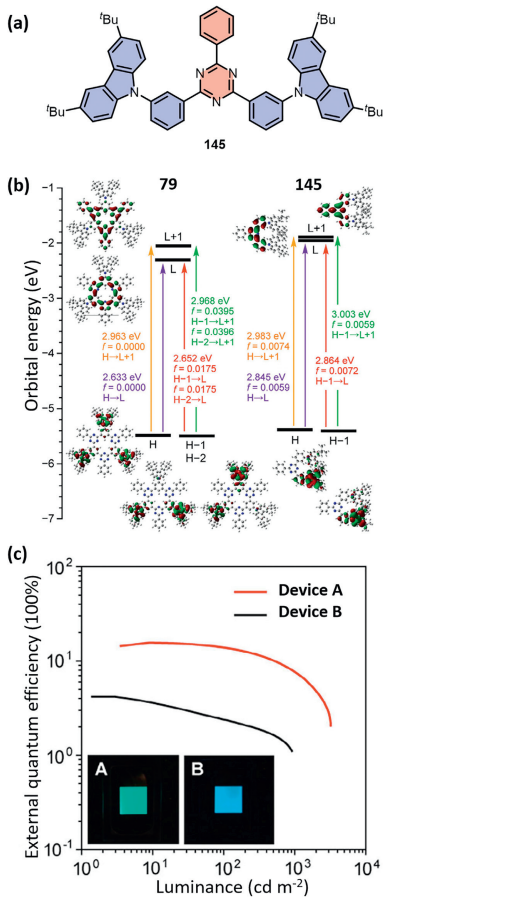

Fig. 52. (a) Structure of acyclic compound **145**; (b) Frontier molecular orbitals of **79** and **145**; (c) External electroluminescence efficiency of OLED devices based on **79** (device A) and **145** (device B). Reproduced with permission [81]. Copyright 2021, WILEY-VCH.

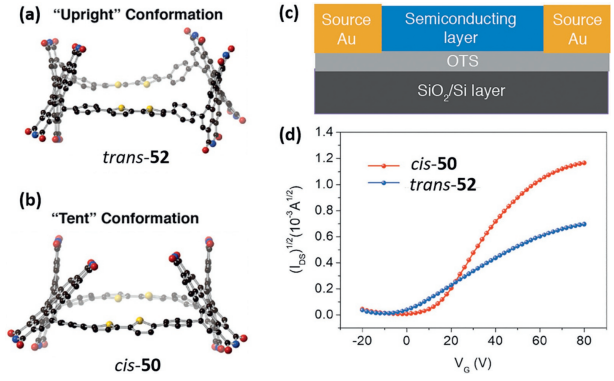

Fig. 53. DFT calculated lowest energy geometry for *cis*-**50** (a) and *trans*-**52** (b); (c) Schematic of the OFET device; (d) Transfer characteristics for *cis*-**50** and *trans*-**52**. Reproduced with permission [75]. Copyright 2018, American Chemical Society.

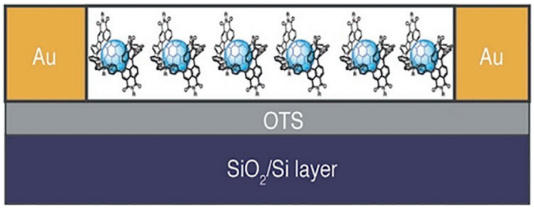

Fig. 54. The (*R*,*R*)-**47**⊃$PC_{61}BM$ complexes used in the active layer of OFET device. Reproduced with permission [106]. Copyright 2020, Wiley online library.

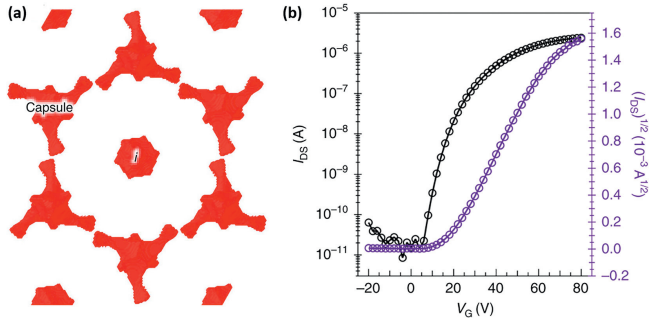

Fig. 55. (a) Surface map of the void space in the ab plane of **48**-Br_{12}; (b) Transfer characteristics of OFET device for **48**-Br_{12}. Reproduce with permission [74]. Copyright 2018, Springer Nature.

sesses interior spaces showed response to different hydrocarbons, which is expected to be applied in sensing and nanoreactors.

6. Conclusions and outlook

In this review, we have presented important works of photoactive donor-acceptor conjugated macrocycles during the past decades, including the synthesis of DACMs with different D, A units and linkage moieties, excellent photophysical properties, intriguing host-guest chemistry, as well as various potential applications especially in chemical sensors, bioimaging, photoelectronic devices. This new emerging class of photoactive DACMs have offered a prospective strategy to combine the bilateral advantages of synthetic macrocycles and D-A molecules, which pave an avenue for the development of supramolecular chemistry and functional materials. Despite the great breakthroughs have achieved in this promising field, there are still issues needed to be solved in the near future: (1) Coupling-based pathways with tedious synthetic steps and low overall yield impede their further applications. One promising strategy is the dynamic covalent methods that the macrocyclization are carried out under thermodynamic control, such as Perkin condensation and alkyne metathesis [66,118]. (2) Diverse building blocks are needed to construct macrocyclic architecture with novel properties and unique functions. (3) Though altered optical and electronic properties of photoactive DACMs provide many possibilities for various applications, more fine modification on structure and property should be taken into consideration in order to enhance their performances as functional materials. The construction of DACMs with suitable inner cavity are anticipated to form host-guest systems, which provides an excellent way to tune self-assembly and are promising to be applied in OSCs. Also, tunable energy gap of DACMs that reflect in photo and redox properties offer the possibility for further applications in organic photoelectronic materials. Moreover, DACMs with high first hyperpolarizability are expected to obtain, which holds great potential in the fields of second-order NLO materials.

The past decades have witnessed the remarkable progress of photoactive DACMs in the synthetic chemistry and supramolecular chemistry. Undoubtedly, the development of D-A π-conjugated macrocycles is still going to flourish and opportunities and challenges coexist in this promising domain. The great potential of photoactive DACMs inspires us spare no efforts to explore and investigate their further application as photofunctional materials.

Declaration of competing interest

The authors declare that they have no known competing financial interests or personal relationships that could have appeared to influence the work reported in this paper.

Acknowledgments

This work is supported by the National Natural Science Foundation of China (Nos. 21971041 and 22001039) and Natural Science Foundation of Fujian Province (No. 2020J01447).

References

[1] Z. Li, Y.W. Yang, Polym. Chem. 12 (2021) 4613–4620.
[2] M. Iyoda, J. Yamakawa, M.J. Rahman, Angew. Chem. Int. Ed. 50 (2011) 10522–10553.
[3] M. Zuo, K. Velmurugan, K. Wang, X. Tian, X.Y. Hu, Beilstein J. Org. Chem. 17 (2021) 139–155.
[4] Y. Zhou, K. Jie, R. Zhao, F. Huang, Adv. Mater. 32 (2020) e1904824.
[5] A.K. Yudin, Chem. Rev. 119 (2019) 9723 9723.
[6] B. Zhao, L. Jiang, Q. Jia, Chin. Chem. Lett. 33 (2022) 11–21.
[7] M.R. Gokel, M. McKeever, J.W. Meisel, et al., J. Coord. Chem. 74 (2021) 14–39.
[8] Z. Duan, F. Xu, X. Huang, et al., Macromol. Rapid Commun. 43 (2021) e2100775.
[9] R.M. Kakhki, M. Rakhshanipour, Arabian J. Chem. 12 (2019) 3096–3107.
[10] S. Zhang, I. Boussouar, H. Li, Chin. Chem. Lett. 32 (2021) 642–648.
[11] E. Fenyvesi, T. Sohajda, Environ. Sci. Pollut. Res. Int. 29 (2022) 20085–20097.
[12] N.G. Hädärugä, G.N. Bandur, I. David, D.I. Hädärugä, Environ. Chem. Lett. 17 (2018) 349–373.
[13] D. Duchene, A. Bochot, Int. J. Pharm. 514 (2016) 58–72.
[14] Y. Zhou, J. He, J. Lu, Y. Liu, Y. Zhou, Chin. Chem. Lett. 31 (2020) 2623–2626.
[15] V. Desai, M. Panchal, S. Dey, F. Panjwani, V.K. Jain, J. Fluoresc. 32 (2021) 67–79.
[16] R. Basilotta, D. Mannino, A. Filippone, et al., Molecules 26 (2021) 3963–3977.
[17] V. Guerineau, M. Rollet, S. Viel, et al., Nat. Commun. 10 (2019) 113–127.
[18] R. Cen, M. Liu, J. Lu, et al., Chin. Chem. Lett. 33 (2022) 2469–2472.
[19] Y.H. Liu, Y.M. Zhang, H.J. Yu, Y. Liu, Angew. Chem. Int. Ed. 60 (2020) 3870–3880.
[20] S. Funk, J. Schatz, J. Incl. Phenom. Macrocycl. Chem. 96 (2019) 1–27.
[21] J. Vázquez, M.A. Romero, R.N. Dsouza, U. Pischel, Chem. Commun. 52 (2016) 6245–6248.
[22] J.F. Chen, J.D. Ding, T.B. Wei, Chem. Commun. 57 (2021) 9029–9039.
[23] L. Chen, Y. Cai, W. Feng, L. Yuan, Chem. Commun. 55 (2019) 7883–7898.
[24] M. Xue, Y. Yang, X. Chi, Z. Zhang, F.H. Huang, Acc. Chem. Res. 45 (2012) 1294–1308.
[25] P. Li, Y. Chen, Y. Liu, Chin. Chem. Lett. 30 (2019) 1190–1197.
[26] N.M. Randell, C.L. Radford, J. Yang, et al., Chem. Mater. 30 (2018) 4864–4873.
[27] A.E. London, L. Huang, B.A. Zhang, et al., Polym. Chem. 8 (2017) 2922–2930.
[28] T. Marszalek, M. Li, W. Pisula, Chem. Commun. 52 (2016) 10938–10947.
[29] D.R. Corrochano, A. de la Hoz, A.M. Sánchez-Migallón, R. Caballero, J.R. Ramírez, J. Clean. Prod. 118 (2016) 223–228.
[30] Q. Wu, D. Deng, K. Lu, Z.X. Wei, Chin. Chem. Lett. 28 (2017) 2065–2077.
[31] J. Guo, Y. Zhen, H. Dong, W. Hu, J. Mater. Chem. C 9 (2021) 16843–16858.
[32] Z. Chen, W. Li, Y. Zhang, et al., J. Phys. Chem. Lett. 12 (2021) 9783–9790.
[33] J. Lee, S.M. Lee, S. Chen, et al., Adv. Mater. 31 (2019) 1804762.
[34] X. Lv, W. Li, M. Ouyang, et al., J. Mater. Chem. C 5 (2017) 12–28.
[35] S. Wood, J.H. Kim, J. Wade, et al., J. Mater. Chem. C 4 (2016) 7966–7978.
[36] A. He, Y. Qin, W. Dai, D. Zhou, J. Zou, Chin. Chem. Lett. 30 (2019) 2263–2265.
[37] J. Liu, X. Zhang, J. Zhang, et al., ACS Appl. Mater. Interfaces 14 (2022) 24575–24582.
[38] Y. Li, X. Fan, Y. Li, et al., ACS Nano 16 (2022) 3323–3331.
[39] J. Hu, M. Wu, X. Zhao, et al., Dyes Pigm. 198 (2022) 110034.
[40] D.L. Crossley, L. Urbano, R. Neumann, et al., ACS Appl. Mater. Interfaces 9 (2017) 28243–28249.
[41] T. Han, X. Gu, J.W.Y. Lam, et al., J. Mater. Chem. C 4 (2016) 10430–10434.
[42] Z. Cheng, T. Zhang, W. Wang, et al., Chin. Chem. Lett. 32 (2021) 1580–1585.
[43] M.A. Boles, M. Engel, D.V. Talapin, Chem. Rev. 116 (2016) 11220–11289.
[44] M.A. Majewski, T. Lis, J. Cybińska, M. Stępień, Chem. Commun. 51 (2015) 15094–15097.
[45] J. Luo, Q. Yan, Y. Zhou, et al., Chem. Commun. 46 (2010) 5725–5727.
[46] N. Baser-Kirazli, R.A. Lalancette, F. Jäkle, Angew. Chem. Int. Ed. 59 (2020) 8689–8697.
[47] C. Chochos, N. Tagmatarchis, V. Gregoriou, RSC Adv. 3 (2013) 7160–7181.
[48] S.E. Lewis, Chem. Soc. Rev. 44 (2015) 2221–2304.
[49] M. Iyoda, H. Shimizu, Chem. Soc. Rev. 44 (2015) 6411–6424.
[50] S.S. Zade, M. Bendikov, J. Org. Chem. 71 (2006) 2972–2981.
[51] T. Kawase, H. Kurata, Chem. Rev. 106 (2006) 5250–5273.
[52] L. Zhu, W. Zeng, M. Li, M. Lin, Chin. Chem. Lett. 33 (2022) 229–233.
[53] W.C. Leu, A.E. Fritz, K.M. Digianantonio, C.S. Hartley, J. Org. Chem. 77 (2012) 2285–2298.
[54] C. Li, C. Wang, Y. Guo, et al., J. Mater. Chem. C 7 (2019) 3802–3810.
[55] S. Eder, D.J. Yoo, W. Nogala, et al., Angew. Chem. Int. Ed. 59 (2020) 12958–12964.
[56] K. Shirahata, M. Takashika, K. Hirabayashi, et al., J. Org. Chem. 86 (2021) 302–309.
[57] L. Sturm, F. Aribot, L. Soliman, H. Bock, F. Durola, Eur. J. Org. Chem. (2022) 7–10.
[58] A. Robert, P. Dechambenoit, E.A. Hillard, H. Bock, F. Durola, Chem. Commun. 53 (2017) 11540–11543.

[59] A. Robert, P. Dechambenoit, H. Bock, F. Durola, Can. J. Chem. 95 (2017) 450–453.
[60] G. Naulet, A. Robert, P. Dechambenoit, H. Bock, F. Durola, Eur. J. Org. Chem. (2018) 619–626.
[61] L.Y. Zhu, H.M. Chen, Y.M. Li, M.J. Lin, Dyes Pigm. 198 (2022) 110031.
[62] Y. Jin, C. Yu, R.J. Denman, W. Zhang, Chem. Soc. Rev. 42 (2013) 6634–6654.
[63] M. Mastalerz, Angew. Chem. Int. Ed. 49 (2010) 5042–5053.
[64] S. Lahiri, J.L. Thompson, J.S. Moore, J. Am. Chem. Soc. 122 (2000) 11315–11319.
[65] U.H.F. Bunz, Chem. Rev. 100 (2000) 1605–1644.
[66] W. Zhang, J.S. Moore, Angew. Chem. Int. Ed. 45 (2006) 4416–4439.
[67] P.N.W. Baxter, J. Org. Chem. 69 (2004) 1813–1821.
[68] B. Traber, T. Oeser, R. Gleiter, Eur. J. Org. Chem. 2005 (2005) 1283–1292.
[69] B.V. Phulwale, S.K. Mishra, C. Mazal, Tetrahedron 74 (2018) 3616–3623.
[70] S.K. Keshri, A. Takai, T. Ishizuka, T. Kojima, M. Takeuchi, Angew. Chem. Int. Ed. 59 (2020) 5254–5258.
[71] J.M. dos Santos, L.K. Jagadamma, J. Cameron, et al., J. Mater. Chem. C 9 (2021) 16257–16271.
[72] M. Ball, B. Fowler, P. Li, et al., J. Am. Chem. Soc. 137 (2015) 9982–9987.
[73] C. Liu, G. Yang, Y. Si, Y. Liu, X. Pan, J. Mater. Chem. C 5 (2017) 3495–3502.
[74] B. Zhang, R.H. Sanchez, Y. Zhong, et al., Nat. Commun. 9 (2018) 1957.
[75] M.L. Ball, B. Zhang, Q. Xu, et al., J. Am. Chem. Soc. 140 (2018) 10135–10139.
[76] K. Bold, M. Stolte, K. Shoyama, et al., Angew. Chem. Int. Ed. 61 (2022) e202113598.
[77] K. Bold, M. Stolte, K. Shoyama, et al., Chem. Eur. J. 28 (2022) e202200355.
[78] S.K. Maier, S.S. Jester, U. Muller, W.M. Muller, S. Hoger, Chem. Commun. 47 (2011) 11023–11025.
[79] Y. Li, A. Yagi, K. Itami, J. Am. Chem. Soc. 142 (2020) 3246–3253.
[80] J. Wang, Q. Wan, J. Liu, Chin. J. Chem. 39 (2021) 2705–2710.
[81] S. Shikita, G. Watanabe, D. Kanouchi, J. Saito, T. Yasuda, Adv. Photonics Res. 2 (2021) 1–10.
[82] M. Hermann, D. Wassy, B. Esser, Angew. Chem. Int. Ed. 60 (2021) 15743–15766.
[83] T. Kuwabara, J. Orii, Y. Segawa, K. Itami, Angew. Chem. Int. Ed. 54 (2015) 9646–9649.
[84] E.R. Darzi, E.S. Hirst, C.D. Weber, et al., ACS Cent. Sci. 1 (2015) 335–342.
[85] J.M. Van Raden, E.R. Darzi, L.N. Zakharov, R. Jasti, Org. Biomol. Chem. 14 (2016) 5721–5727.
[86] H. Thakellapalli, S. Li, B. Farajidizaji, et al., Org. Lett. 19 (2017) 2674–2677.
[87] T.C. Lovell, Z.R. Garrison, R. Jasti, Angew. Chem. Int. Ed. 59 (2020) 14363–14367.
[88] Z.L. Qiu, C. Tang, X.R. Wang, et al., Angew. Chem. Int. Ed. 59 (2020) 20868–20872.
[89] Z.L. Qiu, M.B. He, K.S. Chu, et al., Adv. Optical Mater. (2021) 2100482.
[90] T. Fan, Y. Zhang, L. Wang, et al., Angew. Chem. Int. Ed. (2022) e202213585.
[91] P. Chen, R.A. Lalancette, F. Jakle, Angew. Chem. Int. Ed. 51 (2012) 7994–7998.
[92] P. Chen, X. Yin, N. Baser-Kirazli, F. Jakle, Angew. Chem. Int. Ed. 54 (2015) 10768–10772.
[93] N. Baser-Kirazli, R.A. Lalancette, F. Jäkle, Organometallics 40 (2021) 520–528.
[94] S.Q. Zhang, Z.Y. Liu, W.F. Fu, et al., ACS Nano 11 (2017) 11701–11713.
[95] S. Izumi, H.F. Higginbotham, A. Nyga, et al., J. Am. Chem. Soc. 142 (2020) 1482–1491.
[96] A.C. Carbonnelle, J. Zhu, Org. Lett. 2 (2000) 3477–3480.
[97] C. Castro, Z. Chen, C.S. Wannere, et al., J. Am. Chem. Soc. 127 (2005) 2425–2432.
[98] S. Yamago, Y. Watanabe, T. Iwamoto, Angew. Chem. Int. Ed. 49 (2010) 757–759.
[99] G. Fuhrmann, T. Debaerdemaeker, P. Bäuerle, Chem. Commun. (2003) 948–949.
[100] D. Zhang, M. Heeney, Asian J. Org. Chem. 9 (2020) 1251 1251.
[101] E.M. Kosower, Acc. Chem. Res. 15 (1982) 259–266.
[102] Z.R. Grabowski, K. Rotkiewicz, W. Rettig, Chem. Rev. 103 (2003) 3899–4032.
[103] M. Ball, Y. Zhong, B. Fowler, et al., J. Am. Chem. Soc. 138 (2016) 12861–12867.
[104] W. Zeng, L.Y. Zhu, Y. Chen, M.J. Lin, Dyes Pigm. 190 (2021) 109324.
[105] S. Zahid, A. Rasool, M. Ans, M. Yaseen, J. Iqbal, Energy Fuels 35 (2021) 15018–15032.
[106] T.A. Barendt, M.L. Ball, Q. Xu, et al., Chem. Eur. J. 26 (2020) 3744–3748.
[107] L. Cheng, X. Peng, S. Zhang, et al., Appl. Surf. Sci. 462 (2018) 1036–1043.
[108] L. Yuan, W. Lin, K. Zheng, L. He, W. Huang, Chem. Soc. Rev. 42 (2013) 622–661.
[109] X.M. Chen, Q. Cao, H.K. Bisoyi, et al., Angew. Chem. Int. Ed. 59 (2020) 10493–10497.
[110] T.E. Stennett, P. Bissinger, S. Griesbeck, et al., Angew. Chem. Int. Ed. 58 (2019) 6449–6454.
[111] W. Zeng, M.H. Lin, L.Y. Zhu, M.J. Lin, Chin. J. Chem. 40 (2021) 39–45.
[112] Z.L. Qiu, M.B. He, K.S. Chu, et al., Adv. Optical Mater. 9 (2021) 2100482.
[113] B. Kan, M. Li, Q. Zhang, et al., J. Am. Chem. Soc. 137 (2015) 3886–3893.
[114] M.T. Dang, L. Hirsch, G. Wantz, Adv. Mater. 23 (2011) 3597–3602.
[115] A. Endo, M. Ogasawara, A. Takahashi, et al., Adv. Mater. 21 (2009) 4802–4806.
[116] X. Liang, Z.L. Tu, Y.X. Zheng, Chem. Eur. J. 25 (2019) 5623–5642.
[117] Z. Yang, Z. Mao, Z. Xie, et al., Chem. Soc. Rev. 46 (2017) 915–1016.
[118] X. Hu, C. Yu, D.O. K, et al., Chem. Commun. 52 (2016) 5848–5851.